Hydrology and
Earth System
Sciences

Exploring the regolith with electrical resistivity tomography in large-scale surveys: electrode spacing-related issues and possibility

Laurent Gourdol[1], Rémi Clément[2], Jérôme Juilleret[1], Laurent Pfister[1], and Christophe Hissler[1]

[1]Catchment and Eco-hydrology Research Group (CAT), Luxembourg Institute of Science
and Technology (LIST), Belvaux, 4422, Luxembourg
[2]REVERSAAL Research Unit, National Research Institute for Agriculture,
Food and Environment (INRAE), Villeurbanne, 69626, France

Correspondence: Laurent Gourdol (laurent.gourdol@list.lu)

Abstract. Within the critical zone, regolith plays a key role in the fundamental hydrological functions of water collection, storage, mixing and release. Electrical resistivity tomography (ERT) is recognized as a remarkable tool for characterizing the geometry and properties of the regolith, overcoming limitations inherent to conventional borehole-based investigations. For exploring shallow layers, a small electrode spacing (ES) will provide a denser set of apparent resistivity measurements of the subsurface. As this option is cumbersome and time-consuming, larger ES – albeit offering poorer shallow apparent resistivity data – is often preferred for large horizontal ERT surveys. To investigate the negative trade-off between larger ES and reduced accuracy of the inverted ERT images for shallow layers, we use a set of synthetic "conductive–resistive–conductive" three-layered soil–saprock/saprolite–bedrock models in combination with a reference field dataset. Our results suggest that an increase in ES causes a deterioration of the accuracy of the inverted ERT images in terms of both resistivity distribution and interface delineation and, most importantly, that this degradation increases sharply when the ES exceeds the thickness of the top subsurface layer. This finding, which is obvious for the characterization of shallow layers, is also relevant even when solely aiming for the characterization of deeper layers. We show that an oversized ES leads to overestimations of depth to bedrock and that this overestimation is even more important for subsurface structures with high resistivity contrast. To overcome this limitation, we propose adding interpolated levels of surficial apparent resistivity relying on a limited number of ERT profiles with a smaller ES. We demonstrate

that our protocol significantly improves the accuracy of ERT profiles when using large ES, provided that the top layer has a rather constant thickness and resistivity. For the specific case of large-scale ERT surveys the proposed upgrading procedure is cost-effective in comparison to protocols based on small ES.

1 Introduction

Within the critical zone, the architecture and properties of the regolith, as well as its distribution across the landscape, play a key role in how rainfall is collected, stored and finally released to generate streamflow (Schoeneberger and Wysocki, 2005; Lin, 2010; Ghasemizade and Schirmer, 2013; Brooks et al., 2015). Factors such as the depth and composition of the soil cover and the rock weathering determine water pathways, storage capacity, residence times in the subsurface and subsequent interactions with surface water bodies (Freer et al., 2002; Hopp and McDonnell, 2009; Graham et al., 2010; Gabrielli et al., 2012; Lanni et al., 2013; Ameli et al., 2016).

However, limited access to the subsurface is a major hurdle to acquiring this information, meaning that often even the most basic data are missing, such as the transitions from the soil to the hard bedrock (Brooks et al., 2015). It is the complexity and spatial variability of the subsurface that make its characterization very challenging. Conventional investigation techniques (i.e. soil pits, drillings) of regolith are known to be invasive and of limited spatial representativeness – a

trait causing them to be ignored in the vast majority of catchment studies (Burt and McDonnell, 2015; Parsekian et al., 2015). Several authors have also recently pointed out the subsurface as being the greatest knowledge gap in the understanding/modelling of hydrological processes, with a greater investment in "seeing" the subsurface needed to provide the Earth system modelling community with critical guidance on how to parameterize model subsurface structure depths and properties (Fan et al., 2019).

Geophysical prospection techniques have received increasing attention in recent years within the hydrological sciences community, thanks to their non-destructive character and ability to provide information on subsurface features over large areas. These investigative tools are now recognized as being essential for accurately characterizing the subsurface and studying water partitioning (Robinson et al., 2008; Loke et al., 2013; Binley et al., 2015; Brooks et al., 2015; Parsekian et al., 2015; Singha, 2017). Among the geophysical prospection techniques at hand, electrical resistivity tomography (ERT) is commonly used to characterize subsurface environments. This well-known technique is based on the injection of an electrical current through a pair of electrodes and the measurement of the resulting electrical potential between a second pair of electrodes along a line of dozens or hundreds of grounded electrodes. Through inversion schemes, ERT data are used to generate 2D and 3D electrical resistivity maps of the subsurface (see e.g. Binley and Kemna, 2005, for a detailed explanation of the ERT method).

The electrical resistivity tomography of the subsurface provides a weighted average of the electrical resistivity of its mineral grains, liquid and air (Archie, 1942; Keller and Frischknecht, 1966; Reynolds, 2011). Constitutive relationships can be used to link electrical resistivity to several properties and states that are of major interest to hydrologists, e.g. textural properties (Tetegan et al., 2012), porosity (Leslie and Heinse, 2013; Comte et al., 2018), hydraulic conductivity (Slater, 2007; Farzamian et al., 2015), water content (Brunet et al., 2010; Alamry et al., 2017) or solute concentrations (Bauer et al., 2006; Comte and Banton, 2007). While these constitutive relationships are essential for reliable hydrological interpretations (Binley et al., 2015), their accuracy largely depends on the resolution of the ERT images (Day-Lewis et al., 2005).

ERT has also been successfully used to characterize regolith architecture by delineating areas showing similar resistivity patterns (Crook et al., 2008; Comte et al., 2012; Leopold et al., 2013; Cassidy et al., 2014; Holbrook et al., 2014; Hübner et al., 2015; Uhlemann et al., 2015; Wainwright et al., 2016; Scaini et al., 2017). An increasing number of studies use automated edge detection approaches to delineate these key interfaces within the subsurface (Nguyen et al., 2005; Hsu et al., 2010; Chambers et al., 2012, 2013, 2014, 2015; Audebert et al., 2014; Ward et al., 2014; Uhlemann et al., 2015; Wainwright et al., 2016; Scaini et al., 2017). However, it has also shown that the application of these methods can fail – even when the true interface is sharp – because of insufficient sensitivity and accuracy in the vicinity of the interface (Chambers et al., 2013, 2014).

Ultimately, the geophysical information on the subsurface that can be derived from ERT investigations, either in terms of geometry or hydraulic properties, may be used to feed process-based hydrological/hydrogeological models in order to improve their rightness/realism in terms of spatial variability (e.g. Mastrocicco et al., 2010; House et al., 2016; Loritz et al., 2017; Comte et al., 2018). However, when resistivity models form the basis for constructing such process-based models, the accuracy of the geophysical information and its interpretation is a critical issue that can lead to seriously wrong models and correspondingly wrong model predictions (Andersen et al., 2013).

The characterization of subsurface properties and the delineation of structural units within it should thus go hand in hand with a suitable resolution of ERT images. Otherwise, the results can be inaccurate (Chambers et al., 2013, 2014; Clément et al., 2009, 2014; Ward et al., 2014). Chambers et al. (2014) emphasize that using ERT to detect thin surficial layers remains challenging. Indeed, when shallow structures are investigated, a small electrode spacing (ES) is required, as it delivers denser and well-discretized measurements of the shallow subsurface (Reynolds, 2011; Chambers et al., 2014). However, for large horizontal ERT surveys, small ESs are often not a viable option, as their implementation remains time-consuming. Depending on the regolith architecture and the size of the investigated area, it is thus challenging if not impossible to balance the requirement for shallow-layer characterization (i.e. smaller ES) against the competing need to cover the area of interest within a reasonable amount of time and cost (i.e. larger ES) (Chambers et al., 2014). Moreover, as shown by Kunetz (1966) or Clément et al. (2009), oversizing the ES might not only be inappropriate for the characterization of thin surface layers, but it may also affect the characterization of deeper layers by causing a depth-based resistivity bias, as a result of the inversion process which can be affected by a lack of shallow data.

In this study, we focus on which ES should be considered to characterize the entire regolith accurately. More specifically, we are concerned whether deep structures are well defined (within the limits of the intrinsic resolution limitation of the ERT method that translates to a drop in resistivity model sensitivity with depth) if the shallow structure is not well sampled (i.e. if a larger ES is used). These issues should be ideally addressed prior to the design of fieldwork campaigns to avoid any misinterpretation of field data. Ultimately, we aim at carefully choosing the ES parameter for adequately disentangling the subsurface architecture and properties (both for the shallow part of the subsurface and for the deeper layers). We intend to increase the potential for large horizontal ERT surveys – based on oversized ES – to equally deliver detailed knowledge on shallow subsurface structures. Within this work, we investigate the following.
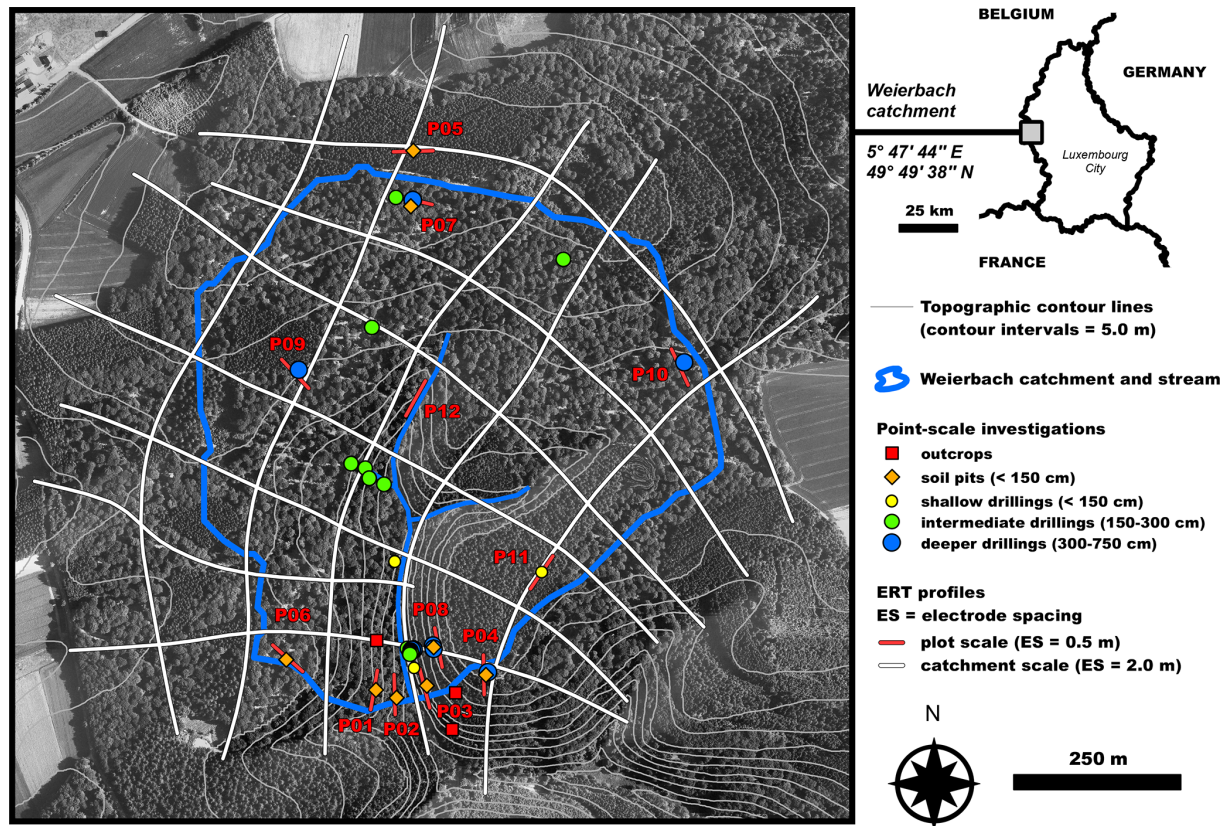
Figure 1. Detailed map of topography and investigations made in the Weierbach catchment (background aerial photography from *Administration du Cadastre et de la Topographie, Luxembourg*).

1. How the inverse solution reconstruction is affected by the ES parameter (i.e. impact of the lack of shallow apparent resistivity data induced by the use of an oversized ES on inverted ERT image accuracy) and which is the most appropriate ES value for accurately characterizing the entire regolith (i.e. for both surface and deeper horizons).

2. The potential for a new approach to improve the accuracy of ERT surveys relying on a large ES by adding interpolated levels of surficial apparent resistivity based on a limited number of measurements with a small ES.

To this end, we use as a reference case study the Weierbach catchment, where an earlier ERT survey has been carried out in order to shed new light on the spatial heterogeneity of the subsurface but for which we have been facing ES choice-related issues. In addition to the field dataset, we investigate a set of synthetic soil–saprock/saprolite–bedrock models using a classical geophysical approach based on numerical modelling to corroborate and reinforce the results. While the former represents a field reality in terms of heterogeneity, the latter provides important information under controlled conditions and a priori exact knowledge. The assessment of the ERT images obtained from these two datasets is carried out

considering the accuracy of the inverted resistivity distribution and the derived interface depths.

2 Materials and methods

2.1 Field study

2.1.1 Study area description

Our experimental test site is the forested Weierbach headwater catchment, located in the Luxembourgish Ardennes Massif ($0.45\,\text{km}^2$; Fig. 1). The geological substratum of the study area is composed of Devonian metamorphic slates. Recent studies in the Weierbach catchment have shown that its regolith plays a key role in runoff generation processes (Pfister et al., 2010; Wrede et al., 2015; Martínez-Carreras et al., 2015, 2016; Scaini et al., 2017, 2018), including lumped-parameter and process-based modelling studies (Fenicia et al., 2014; Glaser et al., 2016, 2019, 2020). Hence, its characterization is of high relevance for gaining new insights into the fundamental catchment functions of water collection, storage and release (Pfister et al., 2017). Several soil pits and drillings were done in the catchment in order to describe its regolith structure and mineralogical and
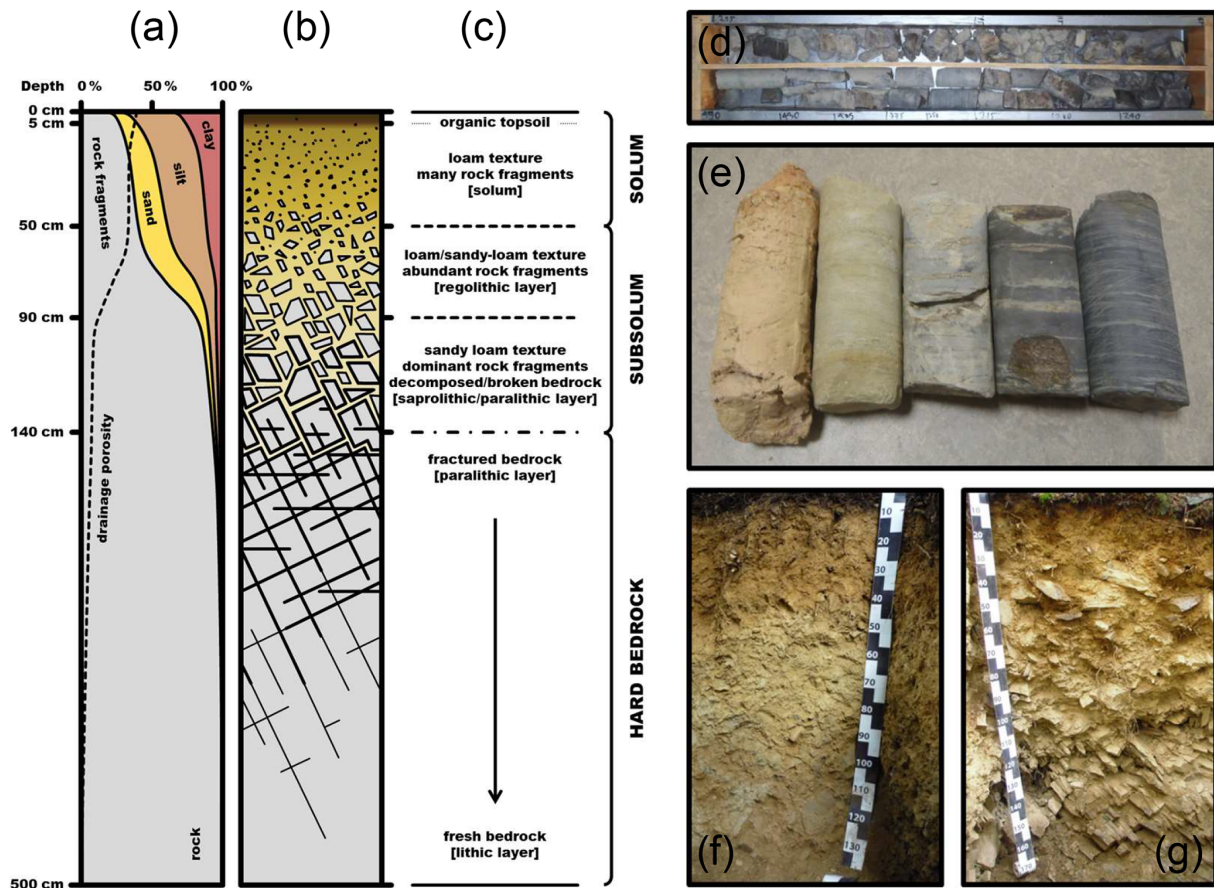
Figure 2. Synthesis scheme of the regolith in the Weierbach catchment (with **(a)** variations with depth of average drainage porosity and rock, sand, silt and clay contents, **(b)** sketch of the regolith and **(c)** description of regolith layers) and pictures of some "point-scale" investigation spots (with **(d)** cores from drilling carried out next to plot-scale ERT profile P04, **(e)** various aspects of the top of the substratum as revealed in deeper drillings, **(f)** soil pit dug next to plot-scale ERT profile P08 and **(g)** soil pit dug next to plot-scale ERT profile P07).

chemical properties (Fig. 1). Based on the visual inspection of soil pits and core drillings and particle size distribution analysis and porosity measurements (Juilleret et al., 2011, 2016; Wrede et al., 2015; Martínez-Carreras et al., 2016; Moragues-Quiroga et al., 2017; Scaini et al., 2017), Fig. 2a–c show a mean schematic representation of the soil-to-substratum continuum. According to rock weathering and pedological processes (Velde and Meunier, 2008; Juilleret et al., 2016), this structure can be partitioned into three main units characterized as follows.

1. The solum is a stony loam soil with a mean thickness of 50 cm. The loam texture stems from a loess deposit, which was mixed through solifluction with many slate clasts native from the bedrock (coarse element content around 25 %). The solum has a high drainage porosity of 30 % on average.

2. The subsolum has two parts. The upper subsolum (from 50 to 90 cm depth on average) is a loam to sandy-loam texture layer with abundant slate fragments. In this part,

the abundance and size of rock fragments strongly increases with increasing depth (coarse element content increases from 30 % to 75 %). Inversely, the drainage porosity decreases, from 30 % to 10 %. The lower subsolum (from 90 to 140 cm depth on average), with the largest content of slate fragments (coarse element content greater than 80 %), corresponds to the decomposed/broken part of the bedrock.

3. The slate hard bedrock starts, on average, at a depth of 140 cm. At first, very large fractures in the hard bedrock tend to close quickly as the depth increases. At a depth of about 5 m, most fractures are closed and the bedrock can be considered fresh and almost impermeable.

Given this intrusive point-scale investigation knowledge, the solum–subsolum electrical resistivity interface is expected to be sharp, while the subsolum–hard bedrock interface is most probably more gradational. In addition, point-scale observations suggest a probable spatial variability of the subsurface electrical resistivity. Indeed, mirroring mul-

tiple weathering phases in the Luxembourgish Ardennes Massif over geological timescales (Moragues-Quiroga et al., 2017; Demoulin et al., 2018), cores obtained from deep drilling campaigns (Fig. 2d) reveal different weathering degrees in the Weierbach catchment (Fig. 2e). The top of the substratum presents a high weathering degree in the upper part of the basin (north and west of the catchment, morphologically expressed by a plateau). Elsewhere in the catchment, bedrock weathering is less pronounced (on hillslope position and along the eastern limit). This difference also implies contrasted surface-layer properties. As observed in soil pits on the plateau, slate fragments are smaller and less consistent and the clay content of the matrix is higher (Fig. 2f; regolithic saprolite subsolum type as per Juilleret et al., 2016). Elsewhere, soil pits exhibit bigger and more coherent slate fragments and less clay in the matrix (Fig. 2g; regolithic saprock subsolum type as per Juilleret et al., 2016).

2.1.2 ERT survey design, data collection and processing

For a characterization of the subsurface of the entire Weierbach catchment, we built a mesh of several large ERT profiles using the roll-along technique (white lines drawn in Fig. 1, cumulative length of about 12 km). The goal was here to inform on the spatial organization and connectivity of the catchment subsurface in terms of the regolith's weathering state and depth to bedrock and to provide eventually new insights into the substratum further deep. To complete this catchment-wide survey in a reasonable time and meet the targeted objectives (in terms of both horizontal and vertical discretization and depth of investigation), we chose a set-up with an ES of 2 m. In order to characterize more accurately the soil-to-substratum continuum for specific landscape units, we added 12 plot-scale ERT profiles of 120 electrodes each, using a smaller ES of 0.5 m (red lines drawn in Fig. 1). Their locations were chosen according to prevailing local geomorphological characteristics (plateau, steep and gentle hillslope, interfluve, close to riparian zone). These last 12 profiles are the ones that we rely on in this study to address the research objectives related to the lack of shallow apparent resistivity data induced by the use of an oversized ES (with the goal of improving in fine the accuracy of ERT images from the catchment-scale survey dataset).

All measurements were taken with a Syscal Pro 120 (10-channel) resistivity meter from IRIS Instruments with multicore cables attached to stainless steel rod electrodes. A pulse duration of 500 ms and a target of 50 mV for potential readings were set as criteria for the current injection. To ensure a good repeatability, stack numbers were automatically adjusted between 3 and 6, aiming for a maximum SD of 3 % for the repeated measurements. We retained the Wenner–Schlumberger array for the measurements. This option offers good depth determination and spatial resolution (Dahlin and Zhou, 2004). Despite the fact that the Wenner–Schlumberger

reciprocal configuration tends to pick up more noise than the normal configuration (Dahlin and Zhou, 2004), we decided to use it because it offers a quick data acquisition time when using a multi-channel resistivity meter. The measurement sequence contains quadrupoles with internal electrode separations of 1 to 9 times the ES and internal–external electrode distances of 1 to 8 times the internal electrode separations.

To assess data accuracy, we measured however 25 % of the quadrupoles in a normal configuration. Reciprocal error calculation (defined as the percentage standard error in the average of the normal and reciprocal measurements; Wilkinson et al., 2012), together with the analysis of the SDs obtained for the repeated measurements, allows us to characterize the measurements as both very precise and accurate (99.4 % of the SDs do not exceed 1 % and 99.1 % of the reciprocal errors are below 5 %; mean SD and reciprocal error values of 0.10 % and 0.68 %, respectively). Even though the overall quality of the data was good, we applied a cleaning procedure (removal of obvious apparent resistivity outliers and all quadrupoles presenting a measured potential lower than 10 mV or a SD of the repeated measurement higher than 3 %). After raw data processing, more than 99.5 % of the original dataset remained available for each of the 12 profiles.

First, all available processed apparent resistivity data were used for the inversion of each profile. Second, to match the set-up of the catchment-scale survey and document the associated loss in resolution, only quadrupoles measured with an ES of 2 m (or equivalent quadrupoles in terms of external electrode distance) were considered.

2.2 Synthetic resistivity dataset

2.2.1 Conceptual resistivity models

As mentioned previously (see Sect. 2.1.1), for a given geological substratum, and according to rock weathering and pedological processes, the regolith can be partitioned into three main units (Velde and Meunier, 2008; Juilleret et al., 2016), namely, from top to bottom,

1. the solum, which is the "true soil", where pedogenetic processes are dominant,

2. the subsolum, corresponding to weathered materials where the original rock structure is preserved and geogenic processes still dominate (depending on the degree of weathering, the saprock and/or saprolite can be distinguished), and

3. the hard bedrock.

Based on this three-layered subsurface conceptual model, and according to the specificity of the Weierbach catchment, we generated 25 1D "conductive solum–resistive subsolum–conductive bedrock" conceptual models to investigate different scenarios with varying resistivity and thickness con-

trasts. Solum and bedrock resistivity was set to $1000\,\Omega\text{m}$ for all models. The solum thickness was also set to a unique value of 0.5 m, which is also in line with the average thickness observed in our study area (see Sect. 2.1.1). To cover a sufficiently wide range of subsurface structures and properties, the subsolum layer was parameterized with several values of thickness (0.5, 1, 2, 4, 8 m) and resistivity (1250, 2500, 5000, 10 000, 20 000 Ωm). The retained resistivity values were also chosen according to the range observed during the field study.

It is worth noting that we have opted for the use of a 1D synthetic model structure but that the subsequent forward modelling and inversion processes will be then done in 2D in order to evaluate not only the accuracy, but also the precision of the inversion results. This would not have been possible using a 1D inversion scheme.

2.2.2 Forward modelling, ERT arrays and electrode spacing

To mimic apparent resistivity measurements with the synthetic models, we simulated the electric field distribution resulting from current injections using the electric field distribution theory (Maxwell's equation) and the finite-element method. We performed numerical simulations using the AC/DC module of Comsol Multiphysics, complemented with a forward 3D modelling (F3DM) MATLAB script (Clément et al., 2011; Audebert et al., 2014). This script assesses automatically, for a quadrupole sequence, the electric potential between the two potential electrodes, for a given current. To achieve a realistic dataset reflecting the properties of a field survey, we applied a systematic Gaussian noise distribution with 3 % SD relative error to the apparent resistivity dataset to simulate the noise commonly recorded with the resistivity meter.

In addition to the Wenner–Schlumberger array which was used for the Weierbach catchment survey, the dipole–dipole array was also used here to simulate apparent resistivity from the resistivity models in order to broaden the modelling findings. The dipole–dipole and Wenner–Schlumberger arrays represent the two most commonly used ERT arrays (Carrière et al., 2017). Their successful application in field studies is mainly due to their surveying efficiency and sensitivity (Dahlin and Zhou, 2004). In order to assess the effect of the lack of shallow apparent resistivity measurements related to the ES choice, simulations of apparent resistivity for both arrays were conducted using five different ESs (0.25, 0.5, 1, 2 and 4 m).

2.3 New approach to upgrade apparent resistivity datasets measured with a large electrode spacing

As exemplified in Fig. 3, the use of a larger ES leads to less apparent resistivity measurements that possibly induce a critical lack of shallow apparent resistivity data. In the event of

an ERT survey carried out with a large ES – and for which the first acquisition level (i.e. quadrupoles whose external electrode separation is of the smallest possible extension; see Fig. 3) is too deep to properly characterize the subsurface structure's top layer (in our case the solum) – we propose to take advantage of the potential relationships between this first acquisition level and additional surficial apparent resistivity acquisition levels (i.e. quadrupoles with smaller external electrode separations; see Fig. 3) obtained from a reduced number of ERT profiles with a smaller ES. If the top layer has a rather constant thickness and resistivity, we consider that such relationships exist and could then be transposed to areas where the larger ES have been used and where data gaps prevail in the shallow subsurface. Illustrated in Fig. 4, this approach may eventually reduce the oversized ES-related effects.

Here, we assess the proposed approach by applying it to the ERT profiles with an ES of 2 m (and obtained from the set of ERT profiles with an ES of 0.5 m), for both synthetic and field datasets, as follows.

1. Step 1 in Fig. 4 – from the set of apparent resistivity data measured with an ES of 0.5 m, we extract the apparent resistivity data corresponding to the first pseudo-depth acquisition level using an ES of 2 m, i.e. quadrupoles with external electrodes separated by 6 m. We then relate each value of this acquisition level to four values of apparent resistivity, located at the same horizontal position (pseudo-x quadrupole location) but relying on the smaller external electrode separations of 1.5, 2.5, 3.5 and 4.5 m, respectively. As in our case quadrupoles with external electrodes separated by 6 m are not in phase with those with the smaller selected external electrode separations (pseudo-x position shifted), we made use of the mean of nearest neighbour values.

2. Step 2 in Fig. 4 – we use the dataset created in the first step to assess (using regression analysis) whether robust relationships exist between the apparent resistivity data of the shallower levels obtained from the external electrode separations of 1.5, 2.5, 3.5 and 4.5 m, respectively, and those obtained with external electrodes separated by 6 m, corresponding to the first acquisition level measured with an ES of 2 m.

3. Step 3 in Fig. 4 – if such relationships exist, we ultimately use them to upgrade the ERT profiles relying on an ES of 2 m. In practice, this implies incorporating into each ERT profile four surficial levels of virtual quadrupoles interpolated from (a) the four regression equations resulting from the second step and (b) the values of its own first acquisition level of apparent resistivity as input of the calibrated relationships.
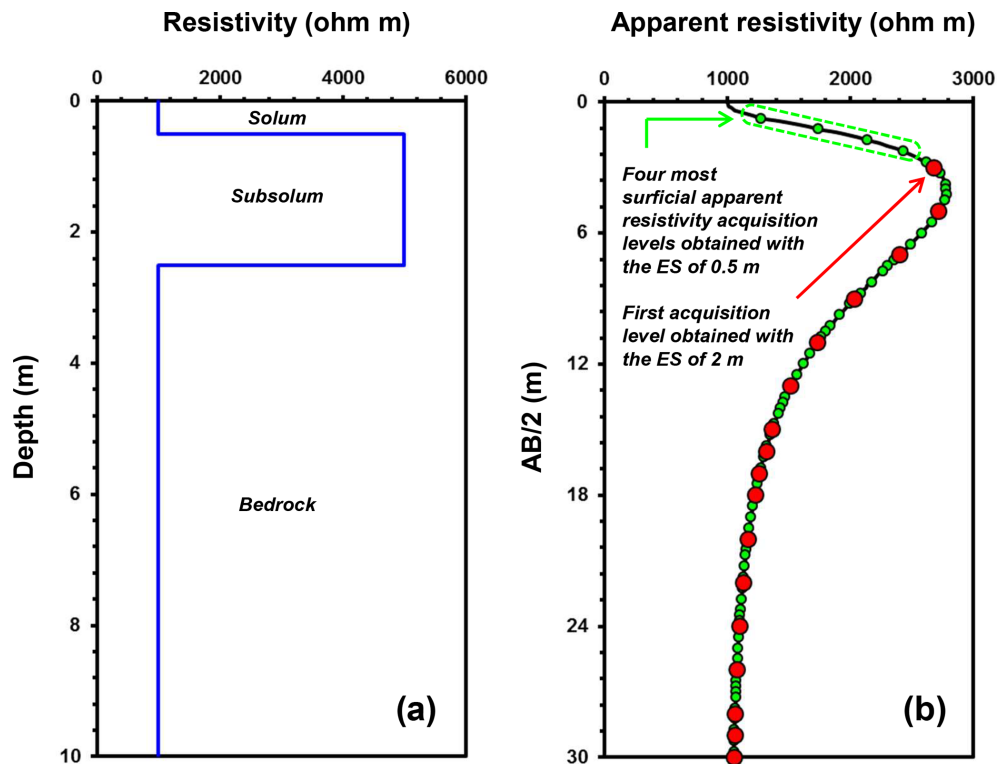
Figure 3. Illustration of the lack of shallow apparent resistivity data posed by the ES parameter-related choice exemplified by **(a)** a 1D geoelectric model (blue line) and **(b)** corresponding Wenner–Schlumberger array apparent resistivity curve (black line) and measurements (green and red dots using, respectively, an ES of 0.5 and 2 m). AB/2 stands for half of the external electrode separations.
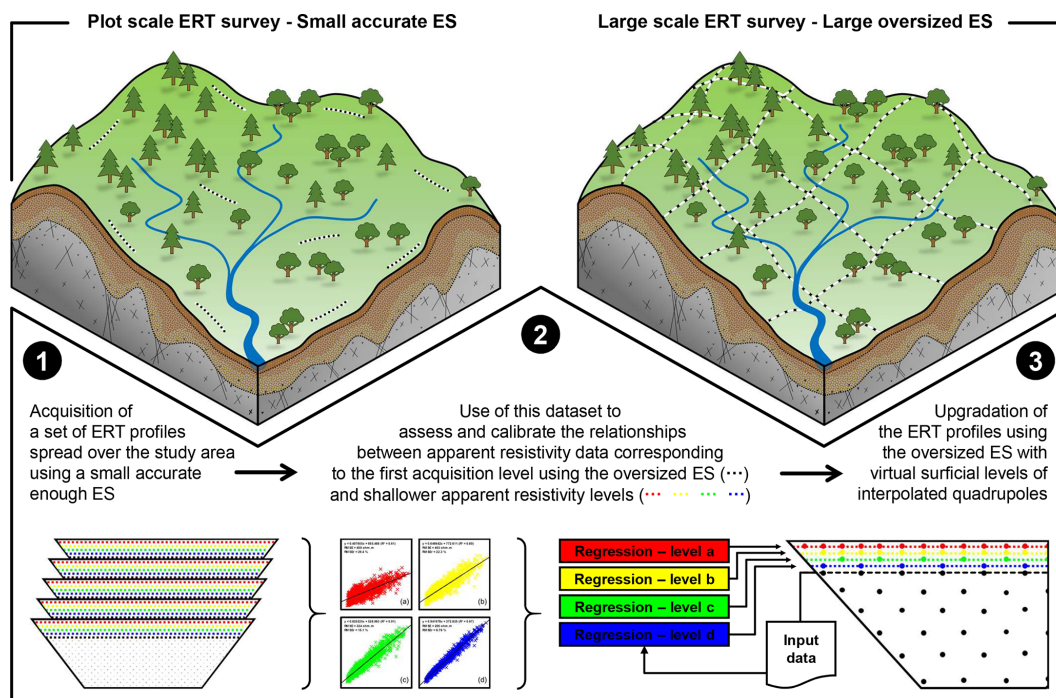

Figure 4. Proposed approach to upgrade ERT datasets relying on a large oversized ES by adding interpolated levels of surficial apparent resistivity based on a limited number of measurements with a small accurate ES.

2.4   Inversion procedure

Both (synthetic and field) datasets were inverted with the same procedure. Inverse solution reconstruction of the interpreted resistivity distribution relied on the BERT code (Boundless Electrical Resistivity Tomography; Günther and Rücker, 2016). This code is based on the finite-element–forward modelling and inversion method described in Rücker et al. (2006) and Günther et al. (2006). The aim of the inversion process is to calculate a resistivity model that satisfies the observed apparent resistivity data. A homogeneous starting model is generated with the median-measured apparent resistivity, for which a response is calculated and compared to the observed data. The starting model is then modified iteratively until an acceptable convergence between the model response and the observed apparent resistivity is achieved. The root mean square misfit error (Loke and Barker, 1996) and the χ^2 criteria (Günther et al., 2006) are used to assess the adequacy between the model response and the observed apparent resistivity. While the root mean square misfit error is the normalized root mean square of the data fit and should be in the range of the relative data error, χ^2 is a measure of how well a model fits the observed data for a given data error, and thus this measure scales with the error.

The constraints placed on the resistivity model during the inversion had to be carefully considered. Here, we used the same 2D inversion settings for all apparent resistivity datasets: a smooth inversion optimization method (L2-norm), a z-weight factor of 1 for generating isotropic resistivity distribution and a regularization parameter λ of 20. In many circumstances, an L1 model constraint with a lower λ value (Loke et al., 2003) would have been preferred for investigating lithological boundaries, since it favours sharp changes in resistivity. But in our case, although the solum–subsolum boundary was expected to be relatively sharp in the Weierbach catchment, the subsolum–hard bedrock interface had a more gradational character. Moreover, the closing with depth of the fractures in the hard bedrock implies also potential smooth changes in resistivity. For those reasons, an L2 model constraint with a moderate λ value was therefore considered to provide a good compromise. Finally, it is important to note that particular care has been taken in discretizing the models. Indeed, following the standard automatic meshing in the inversion code, the larger the ES, the coarser the mesh would have been (Günther and Rücker, 2016). As shallow resolution is the main point of our study, and because inversion results are to a certain degree mesh-dependent, the same fine mesh (whose resolution suits the smallest ES according to Günther and Rücker, 2016) was used for all inversions in order to avoid any coarseness meshing issues in the comparison between the resulting interpreted resistivity images.

2.5   Efficiency criteria for models quality assessment

For the synthetic dataset, we evaluate the agreement between true synthetic resistivity models and interpreted resistivity distributions using the Nash–Sutcliffe model efficiency coefficient (NSE):

$$\text{NSE} = 1 - \frac{\sum_{i=1}^{n}(O_i - P_i)^2}{\sum_{i=1}^{n}\left(O_i - \overline{O}\right)^2}, \tag{1}$$

with O for actual data (true synthetic resistivity values), $\overline{O}$ for mean of actual data, P for calculated data (calculated resistivity from the inversion process) and n for number of data (number of meshes). Originally developed (Nash and Sutcliffe, 1970) and widely used (Bennet et al., 2013; Hauduc et al., 2015; Gupta et al., 2009) for hydrological purposes, the NSE coefficient has also been applied to evaluate the quality of several environmental models, such as geophysical models (Tran et al., 2016).

We compared the true interface depths with those that can be derived from inverted ERT images as an additional way to assess the accuracy of the results. In ERT image analysis, isosurface and derivative methods are the two groups of methods commonly used for this purpose. Here, we retained the group of derivative methods despite it being shown that these methods can fail because of insufficient sensitivity and accuracy in the vicinity of the interface (Chambers et al., 2013, 2014). Indeed, derivative methods represent the most universal way to extract interfaces because their use is relevant in both homogeneous and heterogeneous subsurface contexts (Chambers et al., 2014). It is worth noting also that derivative methods have already been used with success in other ERT studies, even when using an L2-norm (smooth) model constraint (e.g. Hsu et al., 2010; Chambers et al., 2012; Ward et al., 2014). Derivative methods assume that interfaces are located where changes in image properties are at a maximum. These changes can be detected using either the first or second derivatives, targeting maximum gradients or zero values, respectively (Marr and Hildreth, 1980; Torreão and Amaral, 2006; Sponton and Cardelino, 2015). In this study, we used the second derivative of ERT images and targeted zero values (e.g. Hsu et al., 2010) with Paraview software (Ahrens et al., 2005). To be consistent with the inverse solutions delivered by BERT (Günther et al., 2006), we calculated the second derivative on the logarithm of resistivity. Finally, we defined interfaces by following second-derivative zero contour continuity and horizontality as well as the resistivity distribution and its associated gradient (first derivative). Note that the delineation of some interfaces results from the merging of several zero contours to ensure their continuity.

The same accuracy criteria (NSE and interface depths derived from second-derivative zero values) were used for the field dataset of the Weierbach catchment to assess and compare the accuracy of the inverted ERT profiles obtained from the quadrupoles measured with an ES of 2 m (or equivalents

in terms of external electrode distance), when upgraded or not with the four surficial interpolated levels. In this case, inverted ERT profiles, resulting from the full apparent resistivity measurements using an ES of 0.5 m, served as reference models.

3 Results

3.1 Synthetic modelling results

The 300 resistivity models resulting from the inversion of the synthetic resistivity models are provided as supporting information (Figs. S1–S6 and S7–S12 in the Supplement for the Wenner–Schlumberger and dipole–dipole arrays, respectively). Depending on the models, the inversion process was terminated after 1 to 11 iterations. As suggested by the root mean square misfit error (average: 0.89 %, range: 0.40 %– 2.12 %) and the χ^2 criteria (average: 0.81, range: 0.16–4.11), acceptable convergence between the calculated and simulated apparent resistivity data was achieved for all models. In 98 % of all cases, the root mean square misfit error and the χ^2 were less than 1.5 and 2, respectively.

Note that since the results obtained for both arrays are very similar, we only present those obtained from the Wenner–Schlumberger array and that fit the field case study (Figs. 5–7, Tables 1–2). The same figures and tables resulting from analyses carried out on inversion results from the dipole–dipole array have nonetheless also been produced but are provided in the Supplement (Figs. S13–S15, Tables S1–S2 in the Supplement).

3.1.1 Impact of the electrode spacing on models accuracy

The visual examination of the inversion results (Fig. S1) and NSE values (Table 1, Fig. 5) obtained for the smallest ES (0.25 m) indicates an overall good match of the ERT images with synthetic resistivity models serving as benchmarks. The NSE mean value for the 25 synthetic models is 0.61. As suggested by the NSE mean value of 0.55, results for an ES of 0.5 m are slightly less positive (Table 1, Fig. 5). Nonetheless, here again the resistivity distributions obtained from inversions show a good reproduction of the synthetic resistivity models (Fig. S2). Regarding interface delineation, the results obtained from ERT images with ESs of 0.25 and 0.5 m are also good (with a slightly better accuracy when using the smallest spacing) and offer a good reproduction of the solum thickness and depth to bedrock, as revealed by the proximity of estimates with true depths (Table 1, Fig. 5). Considering the 25 synthetic models overall, for ESs of 0.25 and 0.5 m, the mean differences observed for the solum depth are 0.02 and 0.04 m. For depth to bedrock, at ESs of 0.25 and 0.5 m, observed mean differences reach 0.27 and 0.34 m. We note from the results of the two smallest ESs that resistivity and thickness contrasts of the synthetic resistivity models influ-

ence the accuracy of inverted models. Indeed, when the resistivity contrast of the subsolum is too low or too high (i.e. 1250 and 20 000 Ωm), the NSE values are lower (Table 1, Fig. 5). Similarly, the NSE values also indicate slightly worse results when the subsolum is thin (i.e. 0.5 m). Resistivity contrasts also affect the delineation of interfaces. We observed that an increase in the resistivity contrast induces an overestimation effect of the interface depths (Table 1, Fig. 5). This last finding is less obvious at deeper depths to bedrock.

Although the information delivered when using an ES of 1 m is still valid for estimating the synthetic resistivity models, its accuracy is significantly weakened in comparison to that obtained with ESs of 0.25 and 0.5 m (i.e. mean NSE values for the 25 synthetic models of 0.34; Table 1, Fig. 5). The visual examination of the inversion results indicates an increase in local artefacts induced by the resolution degradation (for instance, see inversion results in Fig. S3 when the subsolum resistivity and thickness in the synthetic model are equal to 1250 Ωm and 8 m, respectively). This degradation is mainly restricted to the lowest resistivity contrast and therefore does not explain the general decrease in the accuracy of the results. For the strongest resistivity contrasts, the inversion process leads to relatively well-defined three-layered structures. However, these are shifted down in depth in comparison to the synthetic resistivity models (especially for the solum–subsolum interfaces; Table 1, Fig. 5). For the 25 synthetic models overall, we observed a mean overestimation of 0.33 m for the solum depth. Similarly, the depths to bedrock are overestimated by an average of 0.54 m. When looking at the subsolum characteristics in detail, the deepening effect on the obtained structure is more pronounced as the resistivity of the subsolum is higher and thicker (Table 1, Fig. 5).

Finally, mean NSE values for the 25 synthetic models obtained from ERT images using ESs of 2 and 4 m are close to and less than zero (0.00 and −0.12 for the ESs of 2 and 4 m, respectively). This indicates an overall performance that has not improved, in the first case, and is even worse, in the second case, than when simply using the mean of the synthetic resistivity models. As shown by the inversion results (Figs. S4–S5), several artefacts disturb the quality of ERT images, predominantly (but not exclusively) when the resistivity contrast is low. We also observed that the distinction between solum and subsolum is not obvious, not only when the subsolum is thin, but even more so when the contrast in resistivity is low. In these cases, the NSE value is always lower than zero and, due to the badly resolved structures, interface delineation from the second derivative of the ERT images often results from merging several second-derivative zero contours (Table 1, Fig. 5). The analysis of the derived interface depths clearly shows that the precision of the interfaces is worse (especially for an ES of 4 m as indicated by the large SDs) and, even more importantly, their accuracy with respect to true depths is poor (Table 1, Fig. 5). Taking into consideration all resistivity and thickness contrasts and using ESs of 2 and 4 m, the mean differences observed
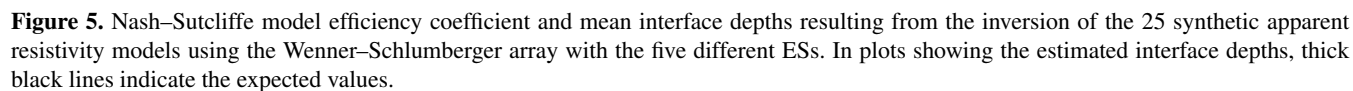
Figure 5. Nash–Sutcliffe model efficiency coefficient and mean interface depths resulting from the inversion of the 25 synthetic apparent resistivity models using the Wenner–Schlumberger array with the five different ESs. In plots showing the estimated interface depths, thick black lines indicate the expected values.

Table 1. Nash–Sutcliffe model efficiency coefficient (NSE) and interface depths (avg ± SD, average ± standard deviation in metres; an italic value specifies that the interface delineation results from the merging of several second-derivative zero contours) resulting from the inversion of the 25 synthetic apparent resistivity models (Tss, subsolum thickness in metres; Rss, subsolum resistivity in Ωm) using the Wenner–Schlumberger array with the five different ESs.

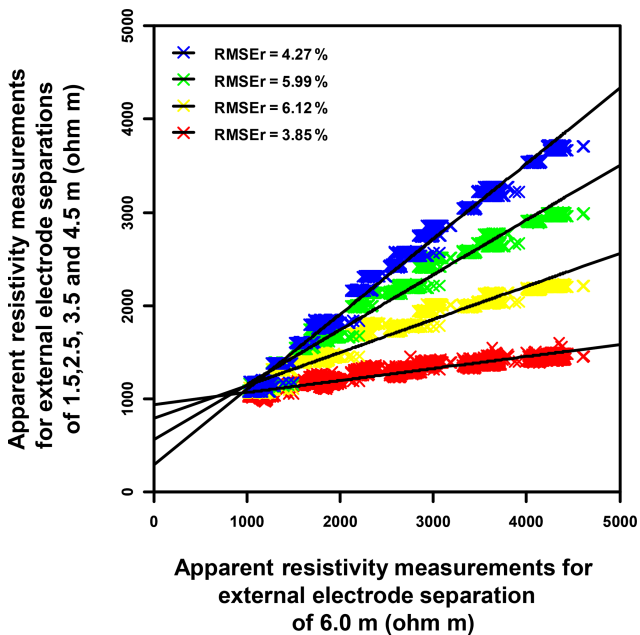| Tss	Rss	ES = 0.25 m			ES = 0.50 m			ES = 1.00 m			ES = 2.00 m			ES = 4.00 m		
		NSE	Solum depth avg ± SD	Depth to bedrock avg ± SD	NSE	Solum depth avg ± SD	Depth to bedrock avg ± SD	NSE	Solum depth avg ± SD	Depth to bedrock avg ± SD	NSE	Solum depth avg ± SD	Depth to bedrock avg ± SD	NSE	Solum depth avg ± SD	Depth to bedrock avg ± SD
0.5	1250	0.16	0.47 ± 0.06	1.30 ± 0.12	0.21	0.37 ± 0.05	1.40 ± 0.16	0.23	0.44 ± 0.09	1.69 ± 0.21	−0.24	*0.28 ± 0.20*	1.49 ± 0.66	0.06	*0.28 ± 0.39*	*2.01 ± 1.33*
0.5	2500	0.48	0.47 ± 0.04	1.37 ± 0.14	0.43	0.39 ± 0.04	1.45 ± 0.14	0.17	0.51 ± 0.04	1.75 ± 0.17	−0.29	*0.21 ± 0.13*	1.60 ± 0.29	−0.05	*0.24 ± 0.32*	*2.43 ± 0.49*
0.5	5000	0.49	0.48 ± 0.04	1.50 ± 0.15	0.45	0.44 ± 0.04	1.59 ± 0.16	0.21	0.59 ± 0.04	1.93 ± 0.19	−0.15	*0.28 ± 0.20*	2.28 ± 0.20	−0.09	*0.18 ± 0.21*	2.43 ± 0.32
0.5	10000	0.45	0.50 ± 0.04	1.67 ± 0.19	0.40	0.51 ± 0.04	1.80 ± 0.20	0.20	0.70 ± 0.05	2.22 ± 0.21	−0.01	0.98 ± 0.06	2.93 ± 0.17	−0.07	*0.25 ± 0.17*	2.69 ± 0.19
0.5	20000	0.37	0.52 ± 0.04	1.91 ± 0.23	0.31	0.58 ± 0.04	2.10 ± 0.24	0.18	0.83 ± 0.06	2.62 ± 0.23	0.12	1.16 ± 0.08	3.40 ± 0.20	0.07	0.52 ± 0.23	3.70 ± 0.30
1	1250	0.51	0.53 ± 0.05	1.59 ± 0.22	0.40	0.55 ± 0.08	1.68 ± 0.19	0.48	0.53 ± 0.09	1.87 ± 0.20	−0.47	*0.29 ± 0.29*	1.78 ± 0.64	−0.32	*0.33 ± 0.31*	2.15 ± 0.89
1	2500	0.69	0.53 ± 0.03	1.69 ± 0.19	0.67	0.51 ± 0.04	1.79 ± 0.19	0.47	0.60 ± 0.04	2.04 ± 0.19	−0.27	0.68 ± 0.14	2.65 ± 0.11	−0.29	*0.26 ± 0.21*	2.42 ± 0.32
1	5000	0.69	0.53 ± 0.03	1.79 ± 0.20	0.65	0.54 ± 0.04	1.92 ± 0.22	0.38	0.70 ± 0.05	2.27 ± 0.22	−0.08	1.01 ± 0.07	2.99 ± 0.17	−0.21	*0.26 ± 0.18*	2.73 ± 0.17
1	10000	0.65	0.54 ± 0.04	1.98 ± 0.23	0.55	0.59 ± 0.04	2.16 ± 0.25	0.26	0.84 ± 0.06	2.65 ± 0.22	0.05	1.17 ± 0.08	3.44 ± 0.20	−0.02	0.55 ± 0.23	3.77 ± 0.31
1	20000	0.56	0.55 ± 0.05	2.25 ± 0.26	0.43	0.65 ± 0.05	2.50 ± 0.30	0.17	0.98 ± 0.07	3.00 ± 0.24	0.15	1.31 ± 0.11	4.02 ± 0.16	0.10	1.48 ± 0.19	5.25 ± 0.40
2	1250	0.50	0.58 ± 0.07	1.98 ± 0.38	0.31	*0.64 ± 0.07*	1.90 ± 0.27	0.53	0.56 ± 0.10	2.08 ± 0.27	−0.38	*0.69 ± 0.44*	2.40 ± 0.88	−0.47	*0.26 ± 0.30*	2.39 ± 0.60
2	2500	0.69	0.54 ± 0.04	2.20 ± 0.29	0.67	0.57 ± 0.05	2.19 ± 0.26	0.53	0.71 ± 0.06	2.49 ± 0.25	−0.02	1.08 ± 0.09	3.23 ± 0.19	−0.29	*0.35 ± 0.20*	3.08 ± 0.21
2	5000	0.68	0.55 ± 0.04	2.32 ± 0.28	0.65	0.59 ± 0.05	2.40 ± 0.28	0.47	0.82 ± 0.07	2.80 ± 0.22	0.13	1.20 ± 0.08	3.60 ± 0.21	−0.10	*0.64 ± 0.27*	4.21 ± 0.34
2	10000	0.65	0.55 ± 0.05	2.50 ± 0.28	0.61	0.63 ± 0.05	2.68 ± 0.26	0.39	0.96 ± 0.06	3.09 ± 0.24	0.19	1.34 ± 0.11	4.12 ± 0.17	0.01	1.61 ± 0.19	5.46 ± 0.42
2	20000	0.62	0.57 ± 0.06	2.79 ± 0.23	0.57	0.68 ± 0.06	2.98 ± 0.24	0.31	1.09 ± 0.08	3.58 ± 0.27	0.10	1.64 ± 0.15	4.76 ± 0.30	0.02	2.41 ± 0.13	6.93 ± 0.44
4	1250	0.63	0.48 ± 0.06	4.34 ± 0.18	0.51	*0.43 ± 0.15*	4.35 ± 0.24	0.17	*0.91 ± 0.37*	3.50 ± 0.24	−0.07	1.06 ± 0.12	3.20 ± 0.20	−0.59	*0.35 ± 0.33*	*2.71 ± 0.97*
4	2500	0.78	0.51 ± 0.04	4.68 ± 0.20	0.73	0.50 ± 0.05	4.70 ± 0.28	0.53	0.75 ± 0.08	3.56 ± 0.32	0.19	1.21 ± 0.10	3.99 ± 0.18	−0.10	1.36 ± 0.33	5.38 ± 0.55
4	5000	0.76	0.52 ± 0.04	4.91 ± 0.23	0.70	0.53 ± 0.06	4.58 ± 0.41	0.51	0.85 ± 0.08	3.65 ± 0.29	0.27	1.36 ± 0.12	4.45 ± 0.25	−0.02	1.96 ± 0.21	6.31 ± 0.57
4	10000	0.70	0.53 ± 0.05	4.67 ± 0.47	0.64	0.58 ± 0.06	4.15 ± 0.55	0.41	1.01 ± 0.07	3.87 ± 0.24	0.19	1.66 ± 0.16	5.07 ± 0.32	−0.03	2.53 ± 0.14	7.29 ± 0.39
4	20000	0.61	0.54 ± 0.06	3.89 ± 0.49	0.57	0.65 ± 0.06	3.99 ± 0.42	0.31	1.16 ± 0.10	4.33 ± 0.29	0.04	1.99 ± 0.18	6.14 ± 0.49	−0.09	2.96 ± 0.17	8.38 ± 0.31
8	1250	0.65	0.46 ± 0.07	9.19 ± 0.33	0.53	*0.34 ± 0.11*	9.52 ± 0.24	−0.19	*1.36 ± 0.25*	10.8 ± 0.30	−0.24	1.15 ± 0.23	3.68 ± 0.33	−0.34	1.55 ± 0.59	5.57 ± 0.77
8	2500	0.78	0.51 ± 0.05	8.33 ± 0.40	0.77	0.48 ± 0.05	8.63 ± 0.25	0.48	0.86 ± 0.10	9.35 ± 0.27	0.23	1.30 ± 0.17	4.26 ± 0.28	−0.07	2.11 ± 0.39	7.33 ± 0.47
8	5000	0.75	0.52 ± 0.05	*9.21 ± 0.93*	0.74	0.53 ± 0.05	8.67 ± 0.26	0.50	0.90 ± 0.07	9.47 ± 0.31	0.22	1.50 ± 0.15	5.04 ± 0.31	−0.02	2.63 ± 0.17	8.41 ± 0.35
8	10000	0.73	0.54 ± 0.05	9.08 ± 0.51	0.71	0.58 ± 0.06	9.20 ± 0.37	0.46	0.98 ± 0.07	9.83 ± 0.53	0.19	1.77 ± 0.15	6.30 ± 0.59	−0.02	2.96 ± 0.16	9.08 ± 0.38
8	20000	0.69	0.54 ± 0.06	9.66 ± 0.36	0.64	0.62 ± 0.06	10.1 ± 0.50	0.40	1.07 ± 0.09	8.92 ± 1.08	0.14	2.04 ± 0.21	7.20 ± 0.48	−0.02	3.32 ± 0.18	9.93 ± 0.50

Figure 6. Scatter plot relating the apparent resistivity data corresponding to the first pseudo-depth acquisition level with an ES of 2 m (external electrode spacing of 6 m) vs. the four surficial apparent resistivity levels using an ES of 0.5 m with external electrode separations of 1.5 (red crosses), 2.5 (yellow crosses), 3.5 (green crosses) and 4.5 m (blue crosses) using the Wenner–Schlumberger array for the 25 synthetic resistivity models. Each point of the scatter plot represents the apparent resistivity of one synthetic model, for the same pseudo-x position, but at different pseudo-depths as defined by the external electrode separation (see Sect. 2.3 for more details). The linear regressions correspond to the thick black lines and their accuracy is indicated by the root mean square relative error (RMSEr).

for the solum indicate an overall overestimation of 0.63 and 0.75 m, respectively. Looking at subsolum characteristic differences, an overestimation of the solum depth is greater as the resistivity of the subsolum is high and is thicker. Furthermore, for low resistivity and thin subsolum, the delimited interfaces of the solum were often characterized by zero depth (Table 1, Fig. 5). Hence, we note a skewing of the mean difference toward negative values. Concerning the depth to bedrock, its estimation is also strongly dependent on the subsolum characteristics of the synthetic resistivity models, leading to a weak and spread correlation with true depths (Table 1, Fig. 5). In most cases, we observed an overestimation. The overestimation increases as the contrast in resistivity in the model becomes larger and the true depth to bedrock gets lower. Conversely, lower resistivity contrasts and deeper true depths to bedrock lead to larger underestimated values.

Table 2. Nash–Sutcliffe model efficiency coefficient (NSE) and interface depths (avg $\pm$ SD, average $\pm$ standard deviation in metres; an italic value specifies that the interface delineation results from the merging of several second-derivative zero contours) resulting from the inversion of the 25 synthetic apparent resistivity models (Tss, subsolum thickness in metres; Rss, subsolum resistivity in Ω m) using the Wenner–Schlumberger array with the ES of 2 m upgraded with the four interpolated levels of surficial apparent resistivity (sil stands for surficial interpolated levels).

		ES = 2.00 m + 4sil		
Tss	Rss	NSE	Solum depth avg $\pm$ SD	Depth to bedrock avg $\pm$ SD
0.5	1250	−1.16	0.35 $\pm$ 0.05	1.23 $\pm$ 0.11
0.5	2500	0.34	0.47 $\pm$ 0.05	1.73 $\pm$ 0.14
0.5	5000	0.33	0.57 $\pm$ 0.04	1.95 $\pm$ 0.20
0.5	10 000	0.30	0.59 $\pm$ 0.04	2.10 $\pm$ 0.23
0.5	20 000	0.27	0.62 $\pm$ 0.05	2.29 $\pm$ 0.27
1	1250	−0.38	0.37 $\pm$ 0.04	1.31 $\pm$ 0.15
1	2500	0.62	0.54 $\pm$ 0.05	2.02 $\pm$ 0.19
1	5000	0.57	0.60 $\pm$ 0.04	2.17 $\pm$ 0.23
1	10 000	0.51	0.61 $\pm$ 0.05	2.34 $\pm$ 0.27
1	20 000	0.43	0.62 $\pm$ 0.05	2.71 $\pm$ 0.26
2	1250	−0.20	0.38 $\pm$ 0.04	1.37 $\pm$ 0.18
2	2500	0.69	0.54 $\pm$ 0.06	2.40 $\pm$ 0.27
2	5000	0.65	0.60 $\pm$ 0.05	2.63 $\pm$ 0.25
2	10 000	0.64	0.60 $\pm$ 0.05	2.88 $\pm$ 0.22
2	20 000	0.61	0.59 $\pm$ 0.06	*3.21 $\pm$ 0.23*
4	1250	−0.04	0.36 $\pm$ 0.04	4.72 $\pm$ 0.32
4	2500	0.70	0.49 $\pm$ 0.06	*3.68 $\pm$ 0.44*
4	5000	0.66	0.54 $\pm$ 0.06	*3.38 $\pm$ 0.28*
4	10 000	0.65	0.55 $\pm$ 0.06	*3.84 $\pm$ 0.47*
4	20 000	0.63	0.57 $\pm$ 0.06	4.47 $\pm$ 0.49
8	1250	−0.76	0.30 $\pm$ 0.06	4.65 $\pm$ 0.19
8	2500	0.62	0.38 $\pm$ 0.08	4.86 $\pm$ 0.46
8	5000	0.68	0.48 $\pm$ 0.07	*7.53 $\pm$ 1.44*
8	10 000	0.68	0.51 $\pm$ 0.07	8.85 $\pm$ 0.58
8	20 000	0.64	0.53 $\pm$ 0.06	8.97 $\pm$ 0.58

3.1.2 Application and assessment of the proposed approach to upgrade ERT datasets

As shown in the scatter plots of Fig. 6, each of the four selected surficial apparent resistivity levels acquired with an ES of 0.5 m (vertical axes) can be derived from the first apparent resistivity acquisition level using an ES of 2 m (horizontal axes) assuming a linear interpolation. As indicated by low root mean square relative error values, the accuracy of each linear regression is good, regardless of the surficial acquisition levels. From the equations of these linear regressions, the resulting four interpolated levels of surficial apparent resistivity were added to the apparent resistivity datasets using the ES of 2 m. ERT images resulting from the inversion of these upgraded datasets are provided in Fig. S6 in the Supple-
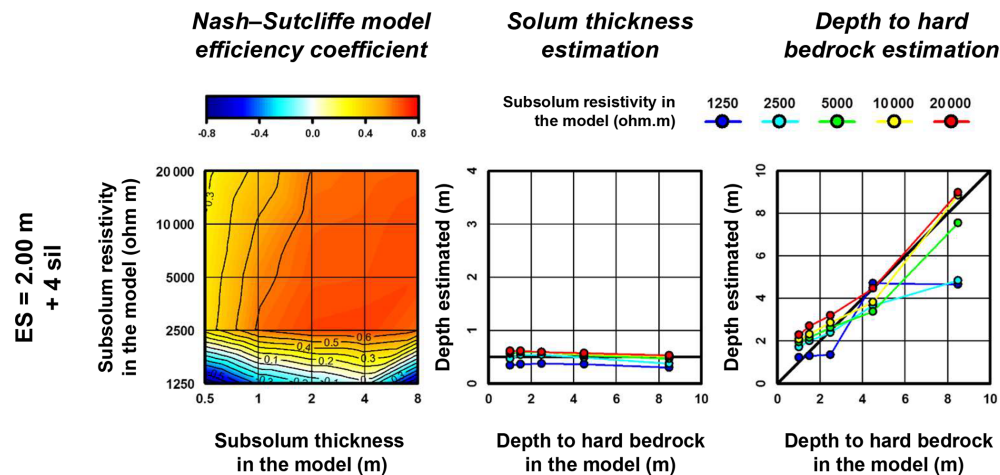
Figure 7. Nash–Sutcliffe model efficiency coefficient and mean interface depths resulting from the inversion of the 25 synthetic apparent resistivity models using the Wenner–Schlumberger array with an ES of 2 m and upgraded with the four interpolated levels of surficial apparent resistivity (sil stands for surficial interpolated levels). In plots showing the estimated interface depths, thick black lines indicate the expected values.

ment. The accuracy criteria, allowing the assessment of their efficiency to reproduce true synthetic models, are shown in Table 2 and Fig. 7.

The visual examination of the inversion results (Fig. S6) and NSE values obtained using the four surficial interpolated levels indicate an overall good match between the ERT images and synthetic resistivity models (Table 2, Fig. 7). The mean NSE value for the 25 synthetic models is equal to 0.35. This value is much better than the one obtained when using the standard apparent resistivity datasets (i.e. 0.00). However, as indicated by negative NSE values, results for the lowest subsolum resistivity contrast (i.e. 1250 Ωm) are of poor quality (Table 2, Fig. 7), especially for the largest depth to bedrock, whose ERT images present strong resistivity artefacts (Fig. S6). These poor results can be linked to the reliability of the linear regressions for models with the lowest resistivity contrast. Indeed, as shown in Fig. 6, regression lines cross each other at low apparent resistivity values and lead to an unsuitable variation of the apparent resistivity. Excluding these models with low resistivity contrasts leads to an increase in the mean NSE value to 0.56, close to the one observed for ERT images relying on an ES of 0.5 m (i.e. 0.60, excluding also models with the lowest resistivity contrasts).

Regarding interface delineation, a strong overall improvement is also observed when adding the four surficial interpolated levels to the apparent resistivity datasets using an ES of 2 m (Table 2, Fig. 7). The precision and accuracy of the interface depths derived from the second derivative of the resulting ERT images are close to the values obtained from the ERT images based on an ES of 0.5 m. Here again, the improvement of the results is notably smaller in the case of the lowest resistivity contrast. It is worth noting that the estimates of the largest depth to bedrock are also not satisfactory for subsolum resistivity values of 2500 Ωm.

3.2   Field case study

The inversion results obtained for the 12 ERT profiles from the Weierbach catchment, with the two standard apparent resistivity datasets and the upgraded dataset, are presented in Fig. 8. Four to 12 iterations were necessary to achieve the inversion process. In each case, an acceptable convergence between the calculated and simulated apparent resistivity data was reached, as indicated by the root mean square misfit error (average: 2.54 %, range: 0.94 %–4.82 %) and the χ^2 criteria (average: 1.18, range: 0.39–3.08). For each ERT profile, the median resistivity patterns as a function of depth, as well as the median estimates of solum thickness and depth to hard bedrock derived from the second derivative of ERT images, are provided in Fig. 9.

3.2.1   Description of ERT results obtained using an electrode spacing of 0.5 m

As shown in Figs. 8a and 9 (blue thick lines), the variability of resistivity with depth obtained using an ES of 0.5 m correctly reflects the Weierbach catchment subsurface structure. Overall, the observed interpreted resistivity variations are similar for each of the 12 profiles. First, at a depth of less than 0.5 m, the solum has a relatively low resistivity. Then, the resistivity curves form a sharp peak representing the subsolum, rising on average between 0.5 and 1 m depth and declining between 1 and 1.5 m depth. In the range 1.5–5 m of the fractured bedrock, the interpreted resistivity continues to decline, but the decay is less and less steep as the depth increases. From about 5.0 m depth, resistivity becomes relatively stable.

A clear distinction between the different stages of weathering affecting the regolith is also possible, as revealed by
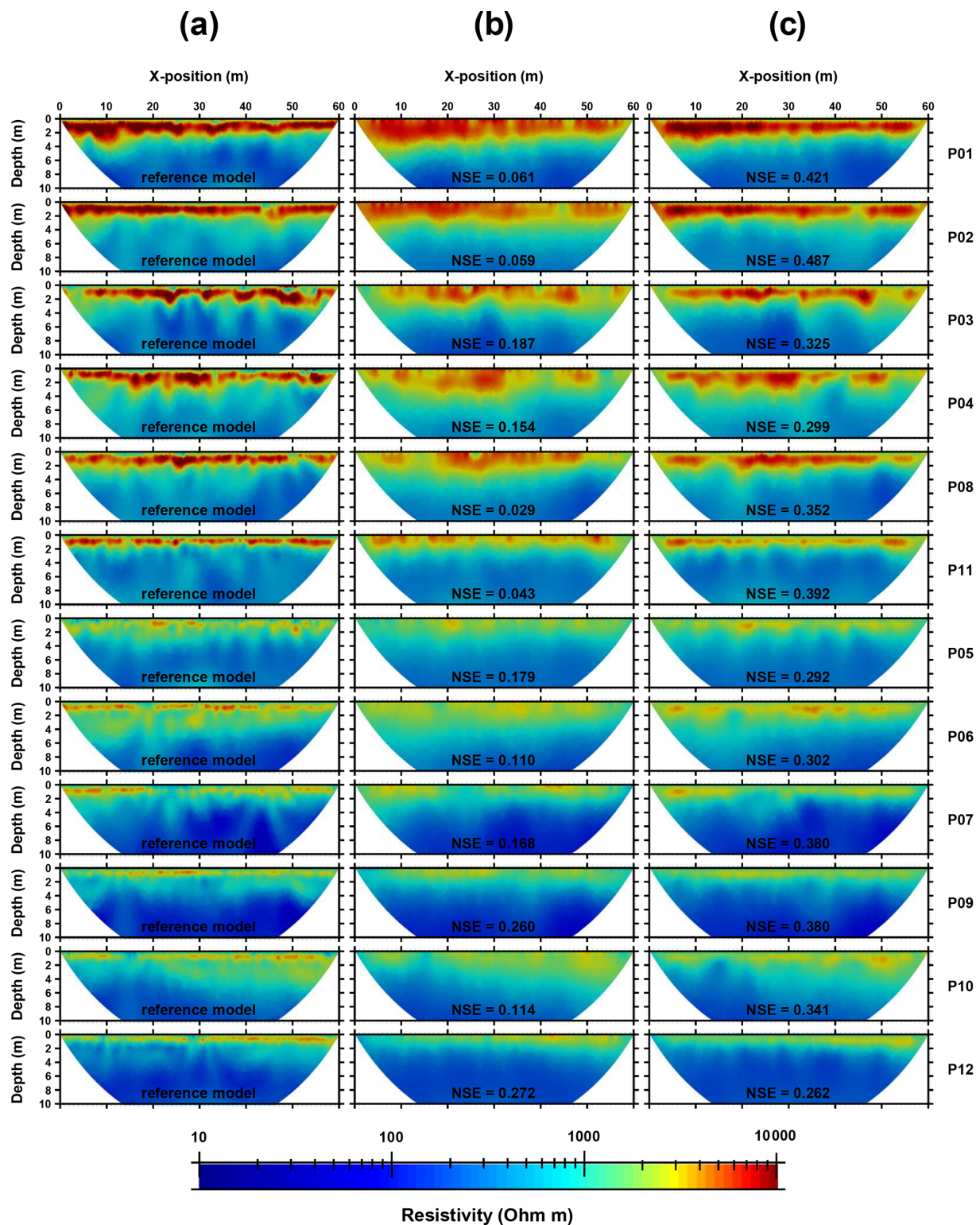
Figure 8. Inversion results obtained for the 12 plot-scale ERT profiles measured in the Weierbach catchment using an ES of 0.5 m **(a)** or 2 m without **(b)** or with the four interpolated levels of surficial apparent resistivity **(c)**. Nash–Sutcliffe model efficiency (NSE) values were added to each ERT image relying on an ES of 2 m using ERT images obtained with an ES of 0.5 m as references.
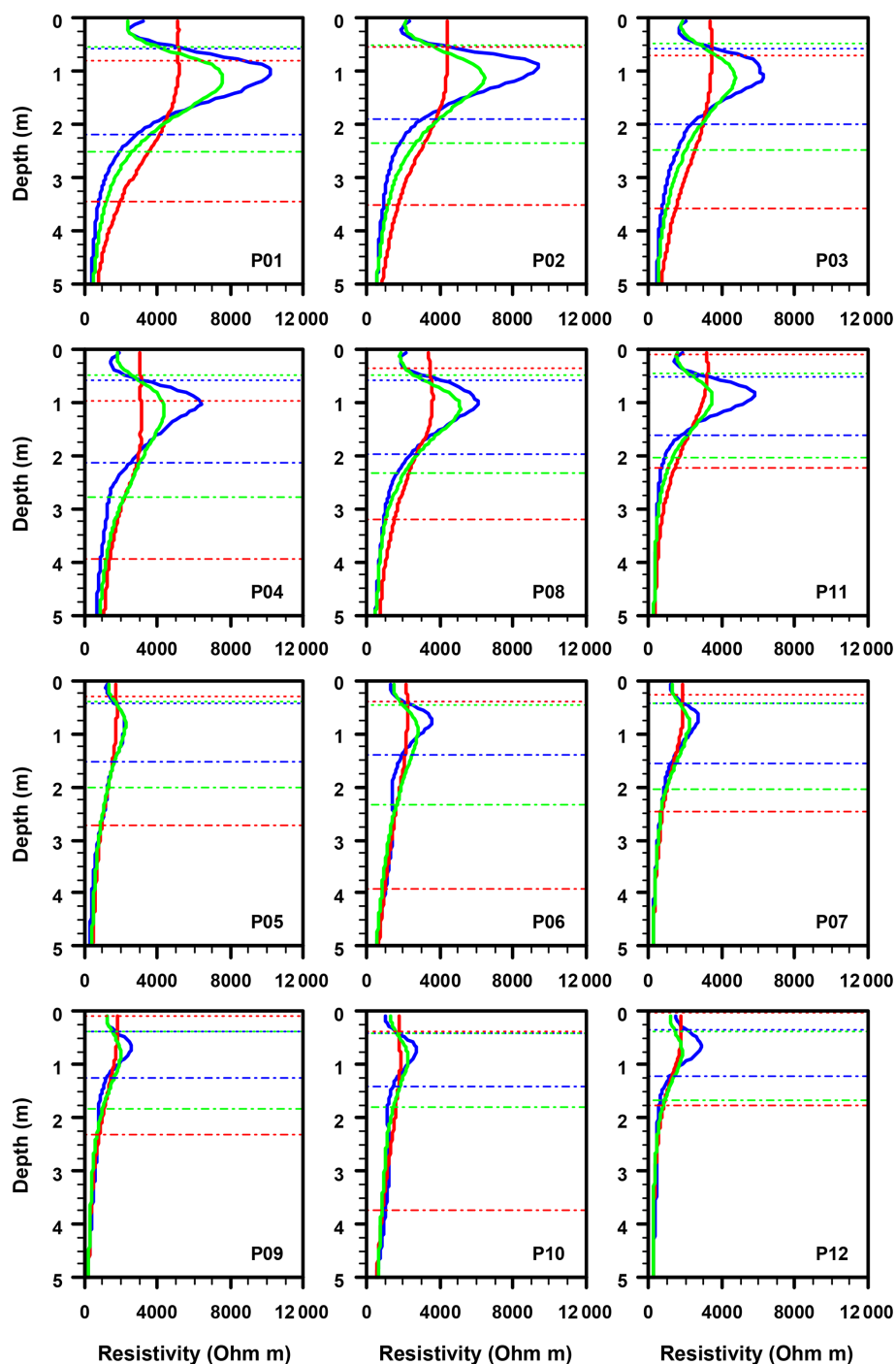
Figure 9. Median resistivity as a function of depth for the 12 plot-scale ERT profiles measured in the Weierbach catchment using an ES of 0.5 m (blue thick curves) or 2 m without (red thick curves) or with the four interpolated levels of surficial apparent resistivity (green thick curves). Median interface depths derived from the second derivative of ERT images are indicated by thin dashed lines for solum thickness and thin dot-dashed lines for depth to hard bedrock (coloured in the same way as the median resistivity curves).

soil pits and drillings. We are able to identify two groups of profiles (Figs. 8a and 9). Profiles P05, P06, P07, P09, P10 and P12, located in the north and the west of the catchment, were characterized by overall lower resistivity values for each of the subsurface layers than profiles P01, P02, P03, P04, P08 and P11, which are located on steep slopes and the eastern catchment boundaries. For instance, the resistivity of the solum ranges from about 1500 to 2000 Ωm for the profiles of the first group and from around 2000 to 3500 Ωm for the profiles of the second group. The peak in resistivity characterizing the subsolum reached values between 2000 and 4000 Ωm for the profiles of the first group. They are much higher, between 5000 and 11 000 Ωm, for the second group. Finally, for the fresh bedrock pattern, the resistivity is of the order of 100–250 Ωm and 250–500 Ω for profiles of the first and second groups, respectively.

Solum thickness and depth to hard bedrock derived from ERT images obtained with an ES of 0.5 m are close to the average estimation values obtained from intrusive investigations (i.e. 0.5 and 1.4 m, respectively; Fig. 2) as shown in Fig. 9 (blue thin dashed and dot-dashed lines) and Table 3, which compiles average values and corresponding SDs (averages of all ERT profiles of 0.48 and 1.78 m, respectively). As we observed in the synthetic modelling exercise in a similar context (mean depth of 2.01 m for 1 m thick subsolum and using the Wenner–Schlumberger array; Table 1), the depth of the bedrock was nonetheless overestimated. Also note that profiles P01, P02, P03, P04, P08 and P11 exhibit thicker solum overall (average value of 0.57 m) as well as deeper hard bedrock (average value of 2.06 m) than profiles P05, P06, P07, P09, P10 and P12 (average values 0.40 and 1.49 m, respectively). Again, this observation is in agreement with the divergence observed as a function of the resistivity contrast through the modelling results.

3.2.2 Comparison of standard and upgraded ERT results obtained using an electrode spacing of 2 m

For all 12 profiles, the scatter plots in Fig. 10 relate the first apparent resistivity acquisition level using an ES of 2 m (horizontal axes) to the first four surficial apparent resistivity levels acquired with an ES of 0.5 m (vertical axes). As with the synthetic modelling results, each of the latter can be derived from the former assuming a linear interpolation. Even if a decreasing accuracy from down to top apparent resistivity levels is noticeable, as indicated by correlation coefficients and RMSE values, the four linear regressions can be qualified as robust and relevant. From the equations of these linear regressions, the resulting four interpolated levels of surficial apparent resistivity were added to the apparent resistivity datasets using the ES of 2 m to build the upgraded datasets.

NSE values comparing standard ERT images obtained with an ES of 2 m and those using an ES of 0.5 m (Fig. 8a and b) clearly suggest an overall decline in geophysical information (mean NSE value of 0.136, range 0.029–0.272), re-

sulting in a biased picture of the subsurface. Indeed, Figs. 8b and 9 (red thick lines) show that in this case, the vertical resolution is insufficient to assess the solum resistivity pattern correctly. Due to this lack of surficial information, the inversion process converges to a solution where solum and subsolum are almost merged into one single layer of intermediate resistivity. As shown in Fig. 11a, this situation leads to a clear overall overestimation of resistivity values in the solum and a reverse underestimation at subsolum levels. Further deep ERT images appear to still be affected since the comparison between resistivity in the fractured bedrock also reveals a non-trivial overestimation. Resistivity values in the fresh bedrock are more accurate, as shown by the distribution of resistivity ratios whose centre is very close to 1.

As shown in Figs. 8c and 9 (green thick lines), the enrichment of the apparent resistivity datasets using an ES of 2 m with the four surficial interpolated levels leads to a better solum–subsolum discrimination in the shallow part. This also allowed a more reliable characterization of the subsurface with depth. Indeed, with the exception of the NSE value of profile P12, which does not vary significantly, all other NSE values (Fig. 8c) indicate that this added surficial constraint is beneficial (i.e. upgraded ERT images obtained with an ES of 2 m better match those using an ES of 0.5 m; mean NSE value 0.353, range 0.2625–0.487). Nonetheless, overall, the inaccuracy remains considerable, as shown by similar dispersion of resistivity ratio distributions, regardless of whether the ERT images were inverted from standard (Fig. 11a) or upgraded (Fig. 11b) apparent resistivity datasets using an ES of 2 m. We associate this with the small vertical resolution and with the loss in horizontal resolution. Nonetheless, the overall bias is lower when adding the four interpolated levels of surficial apparent resistivity (i.e. resistivity ratio distribution more centred on the unit value, regardless of the considered regolith horizon considered; Fig. 11b).

The use of standard ERT images obtained with an ES of 2 m to determine solum thickness leads to less accurate and precise values (see average and SD values in Table 3). Most depth estimates tend towards zero because the vertical resolution is inadequate for correctly distinguishing between solum and subsolum layers (Figs. 12a and 13a). We can nevertheless note that ERT images with higher resistivity contrast lead to an overall better evaluation of the solum thickness (Table 3). This observation is also illustrated in Fig. 13a, where errors have a bimodal distribution with a first peak centred on −0.5 m and a second peak centred on zero. Furthermore, we obtained less accurate and precise estimates of depth to hard bedrock (Table 3 and the width and skew of the distribution of errors observed in Fig. 13a). As clearly shown in Figs. 9, 12a and 13a, the depth to bedrock of each profile is strongly overestimated in comparison with depths derived from ERT images using an ES of 0.5 m (mean overestimation of 1.33 m). Overestimation is greater for ERT images with higher resistivity contrasts (Fig. 12a).

Table 3. Interface depths (avg $\pm$ SD, average $\pm$ standard deviation in metres) derived from the inversion results obtained for the 12 plot-scale ERT profiles measured in the Weierbach catchment using an ES of 0.5 or 2 m (upgraded or not with the four interpolated levels of surficial apparent resistivity; sil stands for surficial interpolated levels). Mean differences (md) in interface depths with the reference ERT images relying on an ES of 0.5 m were added to the standard and upgraded results obtained with an ES of 2 m.

	ES = 2.00 m + 4sil		ES = 2.00 m				ES = 2.00 m + 4sil			
Profile	Solum depth avg $\pm$ SD	Depth to bedrock avg $\pm$ SD	Solum depth avg $\pm$ SD	[md]	Depth to bedrock avg $\pm$ SD	[md]	Solum depth avg $\pm$ SD	[md]	Depth to bedrock avg $\pm$ SD	[md]
P01	0.59 $\pm$ 0.19	2.21 $\pm$ 0.40	0.70 $\pm$ 0.44	[0.11]	3.63 $\pm$ 0.59	[1.42]	0.52 $\pm$ 0.10	[−0.07]	2.55 $\pm$ 0.39	[0.34]
P02	0.54 $\pm$ 0.11	2.01 $\pm$ 0.46	0.59 $\pm$ 0.40	[0.05]	3.44 $\pm$ 0.55	[1.43]	0.50 $\pm$ 0.08	[−0.04]	2.39 $\pm$ 0.32	[0.38]
P03	0.69 $\pm$ 0.31	2.17 $\pm$ 0.67	0.72 $\pm$ 0.45	[0.03]	3.63 $\pm$ 0.97	[1.46]	0.50 $\pm$ 0.13	[−0.19]	2.58 $\pm$ 0.58	[0.41]
P04	0.59 $\pm$ 0.20	2.29 $\pm$ 0.68	0.90 $\pm$ 0.45	[0.31]	3.90 $\pm$ 0.73	[1.61]	0.47 $\pm$ 0.12	[−0.12]	2.74 $\pm$ 0.64	[0.45]
P08	0.52 $\pm$ 0.17	2.04 $\pm$ 0.47	0.43 $\pm$ 0.41	[−0.09]	3.28 $\pm$ 0.65	[1.24]	0.49 $\pm$ 0.12	[−0.03]	2.36 $\pm$ 0.34	[0.32]
P11	0.49 $\pm$ 0.12	1.66 $\pm$ 0.29	0.16 $\pm$ 0.16	[−0.33]	2.25 $\pm$ 0.35	[0.59]	0.46 $\pm$ 0.08	[−0.03]	2.03 $\pm$ 0.27	[0.37]
P05	0.45 $\pm$ 0.20	1.76 $\pm$ 0.61	0.26 $\pm$ 0.20	[−0.19]	2.77 $\pm$ 0.39	[1.01]	0.41 $\pm$ 0.12	[−0.04]	2.02 $\pm$ 0.38	[0.26]
P06	0.41 $\pm$ 0.11	1.42 $\pm$ 0.25	0.38 $\pm$ 0.29	[−0.03]	3.88 $\pm$ 0.73	[2.46]	0.44 $\pm$ 0.11	[0.03]	2.30 $\pm$ 0.53	[0.88]
P07	0.41 $\pm$ 0.14	1.75 $\pm$ 0.50	0.26 $\pm$ 0.26	[−0.15]	2.52 $\pm$ 0.74	[0.77]	0.41 $\pm$ 0.11	[0.00]	1.97 $\pm$ 0.45	[0.22]
P09	0.37 $\pm$ 0.08	1.28 $\pm$ 0.19	0.16 $\pm$ 0.17	[−0.21]	2.35 $\pm$ 0.54	[1.07]	0.39 $\pm$ 0.09	[0.02]	1.84 $\pm$ 0.33	[0.56]
P10	0.41 $\pm$ 0.10	1.46 $\pm$ 0.40	0.52 $\pm$ 0.48	[0.11]	3.80 $\pm$ 1.19	[2.34]	0.41 $\pm$ 0.11	[0.00]	2.11 $\pm$ 0.85	[0.65]
P12	0.34 $\pm$ 0.13	1.25 $\pm$ 0.16	0.11 $\pm$ 0.13	[−0.23]	1.82 $\pm$ 0.35	[0.57]	0.38 $\pm$ 0.09	[0.04]	1.74 $\pm$ 0.30	[0.49]

As for the accuracy of resistivity distributions, the enrichment of the apparent resistivity datasets using an ES of 2 m with the four surficial interpolated levels is also clearly beneficial for the delineation of interface depths. Indeed, Table 3 and Figs. 10 and 12b show that the values obtained for each upgraded ERT profile are closer to those derived from ERT images produced using an ES of 0.5 m for both solum thickness and depth to bedrock. The narrower difference distributions (Fig. 13b), for both solum thickness and depth to bedrock, confirm that results are more precise when adding the four interpolated levels of surficial apparent resistivity. However, while the distribution is centred on 0 in the case of the soil thickness, it is positively shifted for the depth to bedrock. This overestimation with respect to the depths computed when using an ES of 0.5 m, of a mean value of 0.44 m, seems to affect all ERT images, regardless of their resistivity contrast (see Table 3 and Fig. 12b).

4 Discussion

4.1 Inverse solution accuracy issues posed by electrode spacing parameter-related choices

In this study, we investigate a sequence of soil–saprock/saprolite–bedrock. The chosen synthetic three-layered "conductive solum–resistive subsolum–conductive bedrock" structure describes the subsurface of many natural contexts, such as the Weierbach catchment. Through our modelling exercise and the Weierbach catchment case study, we documented the ability and the limitations of ERT to correctly untangle such a typical regolith structure according to the ES parameter. Our results confirm that the choice of

the ES is fundamental for obtaining accurate results, but most importantly it allows us to understand in detail from which ES threshold and why and how the accuracy of the inverted ERT images is affected.

Our results indicate first, for both arrays and whatever the ES retained, that resistivity and thickness contrasts play a key role in the resulting inverted ERT images. In general, for lower resistivity contrasts and shallower structures, the resulting inverted ERT images lead to relatively less well-resolved and fuzzy three-layer structures. Moreover, mainly for the lowest resistivity contrast, local resistivity artefacts are produced and disturb the accuracy of ERT images. At the opposite end of the scale, the higher the resistivity contrast and the deeper the structure, the more the ERT images tend towards a sharp, well-defined three-layered structure in our area of interest. However, in this case, for the strongest resistivity contrasts, the interpreted structures shift in depth, resulting in a decrease in ERT image accuracy. These relationships between resistivity contrasts and interpreted resistivity distributions logically affect the interface depths that are extracted from the second derivative of ERT images.

Our study also emphasizes the critical role of the ESs. The impact of these inverse problem effects as a function of the resistivity and thickness contrasts on the accuracy of the geophysical information delivered does indeed largely depend on the ES parameter. While these effects are rather negligible for the smallest ES, they increasingly deteriorate the accuracy of the ERT images with increasing ES values. More specifically, we observed a threshold effect at an ES value of 0.5 m – as a best compromise to characterize the subsurface. If a larger spacing is retained, the accuracy decreases abruptly in terms of both resistivity distribution and interface
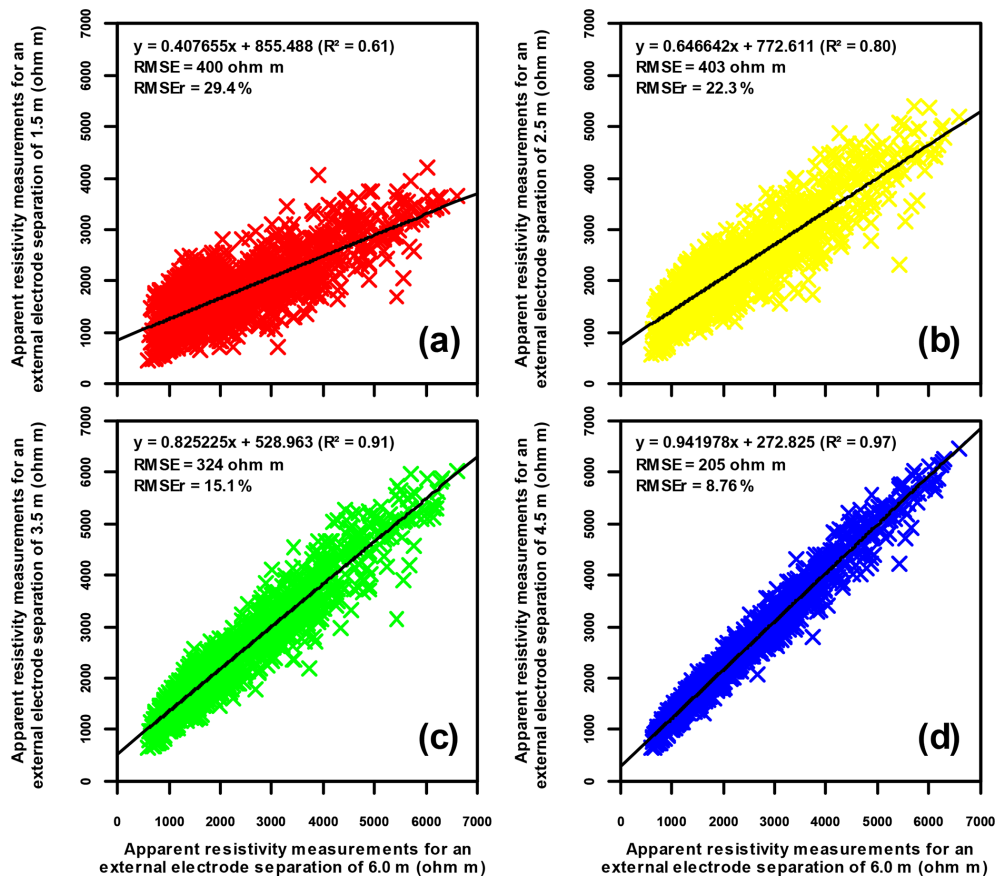
Figure 10. Scatter plots relating the apparent resistivity data corresponding to the first pseudo-depth acquisition level with an ES of 2 m (external electrode spacing of 6 m) vs. the shallower first four surficial apparent resistivity levels using an ES of 0.5 m with external electrode separations of 1.5 (red crosses), 2.5 (yellow crosses), 3.5 (green crosses) and 4.5 m (blue crosses) for the 12 plot-scale ERT profiles measured in the Weierbach catchment. Each point of the scatter plots represents the apparent resistivity of one ERT profile, for the same pseudo-x position, but at different pseudo-depths as defined by the external electrode separation (see Sect. 2.3 for more details). The linear regressions correspond to the thick black lines and their accuracy is indicated by the coefficient of determination (R^2), the root mean square error (RMSE) and the root mean square relative error (RMSEr).

delineation. This finding is valid for both the shallow and deeper horizons of the subsurface. Observations made in the Weierbach catchment fit well this numerical finding. While the use of an ES of 0.5 m gave accurate results, the use of an ES of 2 m produced biased ERT images. In both cases, the ES of 0.5 m corresponds to the thickness of the most surficial layer (i.e. the solum), thus suggesting that the thickness of the solum has to be taken into consideration for the design of ERT surveys.

Indeed, considering the depth of investigation of collinear symmetrical four-electrode arrays using the dipole–dipole or Wenner–Schlumberger arrays (Roy and Apparao, 1971; Barker, 1989), this ES allows a vertical resolution for the shallow parts of the subsurface of about 0.25 m, which corresponds to half the thickness of the uppermost layer. Thus, our results suggest that such a resolution is required. If a larger ES is chosen, the more superficial apparent resistivity measurements are too deep to accurately grasp the sur-

face layer. This oversizing also affects the characterization of deeper layers by causing a depth-based resistivity bias. This last observation supports previous findings (e.g. Kunetz, 1966; Clément et al., 2009) and allows also a better understanding of some biases observed for deep layers in previous studies in terms of both resistivity distribution and interface depth delineation using derivative methods (Meads et al., 2003; Hirsch et al., 2008; Chambers et al., 2014).

Recently, Chambers et al. (2014) highlighted the very significant challenges in using ERT to detect thin surface layers and suggested that a reliable resolution of surface layers with a thickness of less than one-third of ES should not be expected. This conclusion was based on the interface delineation accuracy but not on that of the resistivity distribution. Moreover, the use of derivative methods had failed in their case, and only isosurface methods gave good results. These methods, which consist of selecting a resistivity threshold value on the basis of intrusive measurements
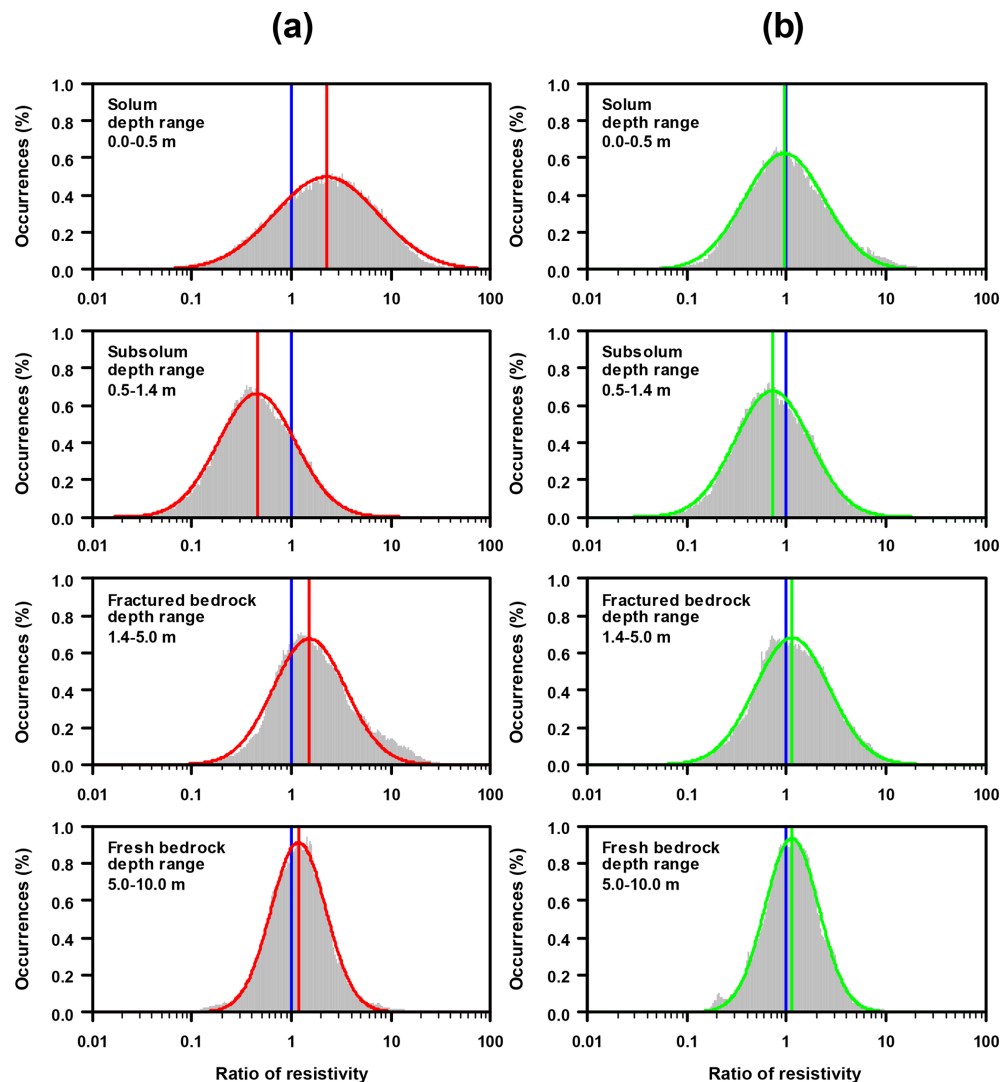
Figure 11. Distribution of the ratios calculated between the inverted resistivities obtained using an ES of 2 m without **(a)** or with the four interpolated levels of surficial apparent resistivity **(b)** and those obtained using an ES of 0.5 m considering the overall 12 plot-scale ERT profiles measured in the Weierbach catchment and discretized by relevant depth horizons. A lognormal distribution, whose centre is indicated by a vertical line, has been fitted for each histogram; the more the distribution is centred and narrowed on the unit ratio (vertical blue lines), the better the adequacy with ERT images using an ES of 0.5 m.

(Chambers et al., 2013, 2014; Wainwright et al., 2016) or using statistical analysis of the ERT images (Audebert et al., 2014; Ward et al., 2014), are indeed less dependent on the sensitivity of ERT images and have shown a greater ability than derivative methods in several cases (Ward et al., 2014; Chambers et al., 2013, 2014). The success of the application of isosurface methods is however restricted to specific case studies, resulting from the homogeneity of targeted resistivity layers which imply consistent interfaces (Chambers et al., 2013, 2014; Ward et al., 2014). In other cases, they provide poor results (Ward et al., 2014; Chambers et al., 2012). Our results are therefore not contradictory with the findings of Chambers et al. (2014).

We ideally recommend using an ES that is close to the thickness of the top subsurface layer in ERT surveys to mirror the architecture and properties of the subsurface correctly. This choice, which is obvious for the characterization of the shallower layer, is also relevant for characterizing the subsurface in its entirety – even when solely aiming for the characterization of deeper layers. However, this recommendation results from one typical subsurface structure and should consequently be transposed to areas of similar characteristics. This means that a generalization of our findings and their interpretation about the inverse solution accuracy problem posed by ES parameter-related choices is limited. Nevertheless, the same methodology as followed in this work
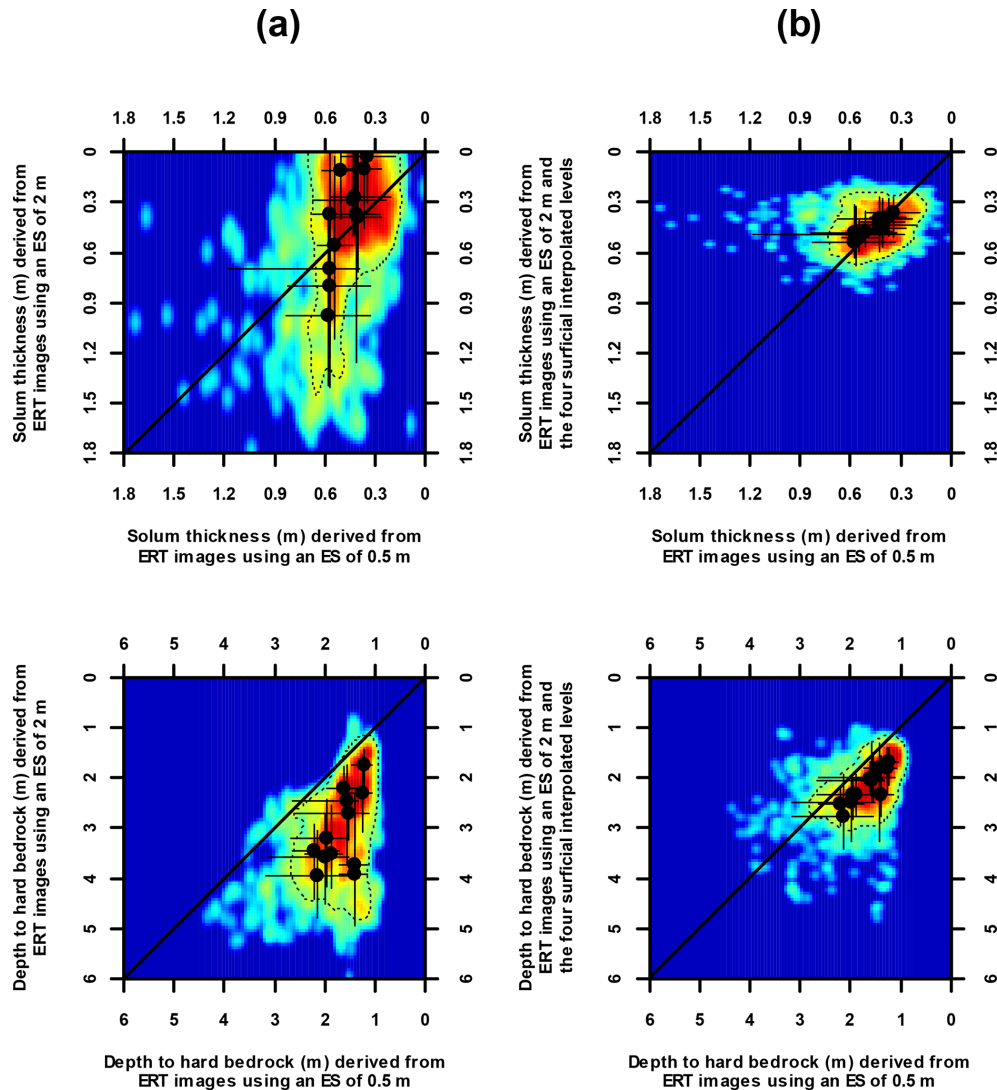
Figure 12. Coloured density scatter plots (red – high density – to blue – low density) showing solum thickness and depth to hard bedrock derived from the 12 plot-scale ERT profiles measured in the Weierbach catchment using an ES of 0.5 m vs. those using an ES of 2 m without (**a**) or with the four interpolated levels of surficial apparent resistivity (**b**). Median values and interpercentile ranges of 10 %–90 % of the interface depth of each ERT profile are shown by black dots and thin vertical and horizontal bars. Envelopes defined by thin dashed black contours encompass 80 % of individual pairs of values.

might be used for other case studies, such as for example the reverse case, i.e. "resistive solum–conductive subsolum–resistive bedrock".

4.2 Potential and limitation of the upgrading procedure proposed in this study

The design of an ERT survey consists of a compromise between the need for high resolution for the near-surface layer (which would suggest smaller ESs) and the need to cover the area of interest in a reasonable amount of time and to an investigation depth that is deep enough to reconstruct the architecture of the deeper layer (which would give a preference for larger ESs; Chambers et al., 2014).

Eventually, as proposed by Dahlin and Zhou (2004), a quadrupole sequence of apparent resistivity measurements with decreasing vertical resolution and horizontal scanning in depth can reduce operational time without a drastic loss of accuracy. Moreover, in recent years, there has been substantial development of algorithms dedicated to automatically determining non-conventional electrode configurations (Loke et al., 2013). Those algorithms can lead to inverted ERT images whose resolution is superior to or equal than, respectively, the same or a fewer number of measurements, to those using standard survey designs, as for example Wenner–Schlumberger or dipole–dipole arrays (e.g. Stummer et al., 2004; Furman et al., 2004, 2007; Wilkinson et al., 2006,
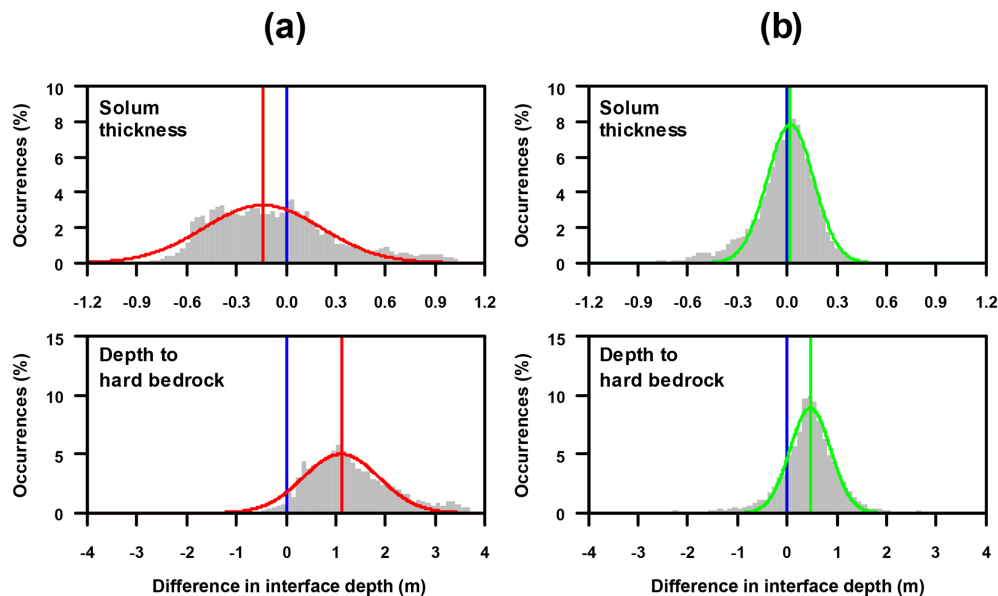
Figure 13. Distribution of differences between interface depths obtained using an ES of 2 m without **(a)** or with the four interpolated levels of surficial apparent resistivity **(b)** and those obtained using an ES of 0.5 m considering the overall 12 plot-scale ERT profiles measured in the Weierbach catchment. A normal distribution, whose centre is indicated by a vertical line, has been fitted for each histogram; the more the distribution is centred and narrowed on the zero value (vertical blue lines), the better the adequacy with interfaces derived from ERT images using an ES of 0.5 m.

2012; Loke et al., 2014; Abdullah et al., 2018; Uhleman et al., 2018). In the scope of large-scale ERT surveys, such optimized non-conventional electrode arrays could also help reduce the operational measurement time without reducing the information content. However, setting up the electrodes remains time-consuming, and the depth of investigation may be insufficient (e.g. ERT device with a limited number of electrodes). If the competing needs to cover the area of interest are still not reached (i.e. cost and time constraints, adequate depth of investigation), a set-up with larger ESs must be preferred, but the accuracy of the resulting ERT images might be affected by inverse solution reconstruction issues related to the lack of shallow apparent resistivity data as documented within this work. An improvement of these results is nevertheless possible by filling the lack of information in the shallow part of the subsurface. For instance, the deployment of a fast-moving measurement device (Andrenelli et al., 2013; Guerrero et al., 2016) could be used in parallel to complement the apparent resistivity dataset. Another example, as shown by Clément et al. (2009), is the use of an advanced inversion constrained by a priori surficial information to improve the accuracy of ERT images.

Both the synthetic and Weierbach catchment datasets demonstrated the potential for our novel upgrading procedure to improve the accuracy of large-scale ERT surveys based on large ESs. By adding four surficial apparent resistivity levels to the standard datasets using an ES of 2 m, we improved the vertical resolution solely in the first metre of the subsurface, as the depth of the investigation curve indicates (Roy and Ap-

parao, 1971; Barker, 1989). However, this focused upgrading led to a better characterization overall in terms of interpreted resistivity distribution and derived interface depths, for both the shallow and deeper horizons of the subsurface. It was this low number of additional data points that improved the solum characterization and its transition with the subsolum, which was missing in the standard apparent resistivity datasets.

The main constraint of the proposed upgrading procedure is that it is only applicable if the shallower layer is relatively homogeneous in terms of resistivity and thickness, which was the case for the synthetic models used. It is indeed this homogeneity that induces the good correlation between the surficial apparent resistivity levels and a deeper level. In the case of the Weierbach catchment, the solum is relatively homogeneous, as indicated by the point-scale investigations available and the 12 plot-scale ERT profiles whose locations were distributed between locations with different geomorphological characteristics. It is important to note that local inconsistencies are expected in places where the shallower part of the subsurface will not satisfy the overall solum homogeneity criteria. For instance, in the riparian zone, where solum and subsolum have been eroded, at forest roads, where the soil has been extensively modified (road cut, ballast), or in grasslands surrounding the catchment, where the soil does not have the same characteristics as in the forest zone, the application of the method would most probably lead to erroneous results by inducing false inverted surficial resistivity layers.

A second limitation of the proposed method is pointed out by the synthetic modelling results. The proposed approach fails and even leads to worse results if there is a low resistivity contrast between layers. Indeed, we were able to show that linear regressions leading to the interpolated levels of surficial apparent resistivity crossed each other in this case and led to an unsuitable variation pattern in the apparent resistivity (Fig. 7). Ultimately, this causes the formation of false resistivity layers by the inversion process (Figs. S6 and S12 in the Supplement). This problem could be solved to some extent by constraining the linear regressions with respect to each other, so that they do not cross. Other improvements of the method can be anticipated, such as a weighting procedure for the inversion of the interpolated levels of surficial apparent resistivity levels, depending on how well they correlate. Relying on a cross-validation to assess the efficiency of the dataset used for the calibration of the regression models for delivering robust estimates of the surficial levels of apparent resistivity would also be beneficial. This statistical method, which relies on splitting the full dataset into two parts, namely the training and validation datasets, is widely used in prediction problems for estimating how accurately a predictive model will perform in practice (Hastie et al., 2008). It would allow for instance assessment of the effect of the dataset size (e.g. number of ERT profiles) and characteristics (e.g. location of the ERT profiles) on the prediction results.

Here again, it is worth recalling that our findings and their interpretation result from one typical subsurface structure. Extra work is needed to strengthen, and eventually adapt, our upgrading approach to a more general regolith pattern. We especially recommend assessing the proposed methodology for the reverse case "resistive solum–conductive subsolum–resistive bedrock". For instance, a set of three-layered "resistive–conductive–resistive" synthetic models might be explored to confirm/infirm the linear regression logic we highlight in this study.

4.3 From the Weierbach catchment perspective and beyond

The ideal design of an ERT survey exploring the architecture and properties of the Weierbach catchment's regolith should rely on an ES of 0.5 m. However, in this configuration, a catchment-scale ERT survey appears totally unrealistic, due to obvious inherent time and cost constraints. Despite their narrow depth of investigation, the use of a fast-moving measurement device might have been a solution to speed up the survey in open landscapes such as grassland or cropland (e.g. Andrenelli et al., 2013; Guerrero et al., 2016), but their deployment in forested areas remains equally cumbersome and time-consuming.

Other geophysical methods exist that might be more efficient than ERT in exploring the regolith over large areas (Binley et al., 2015; Parsekian et al., 2015; Fan et al., 2020).

For instance, ground-penetrating radar (GPR) allows usually a higher spatial resolution and data collection rate. In several studies, GPR has allowed us to accurately delineate interfaces of several relevant structures in the critical zone (e.g. Carrière et al., 2013; Hare et al., 2017; Guo et al., 2019; Šamonil et al., 2020). However, as GPR requires sliding of the instrument on the ground, its use is much more ticklish and time-consuming over long distances in forests than in open areas, such as grassland or cropland. Furthermore, GPR surveys were done in the close vicinity of the Weierbach catchment. The structural analysis only revealed soil layering, but it did not show the depth to bedrock due to chaotic reflection patterns, which are common for this type of geologic setting (Jackisch et al., 2017; Allroggen et al., 2020). The electromagnetic induction (EMI) method could also have been another way to quickly characterize the shallow subsurface at a large scale. Indeed, unlike GPR or ERT, EMI systems do not require a direct coupling with the ground, which allows much faster acquisitions, even in forested areas. Despite their limited spatial resolution and depth of investigation, multi-depth EMI devices have been used in several studies for the characterization of subsurface structures and properties (e.g. Brosten et al., 2011; Saey et al., 2012; Rejiba et al., 2018; Simon et al., 2020). A field test using a multi-frequency domain EMI device (Profiler EMP-400, GSSI) was done in the Weierbach catchment. Unfortunately, the results were inconclusive, as contrasting shallow patterns observed with ERT were in fact not distinguishable due to the overall too electrically resistive nature of the subsurface.

Hence, the upgrading procedure proposed in this study is particularly interesting in the context of the Weierbach catchment. Through our study, we demonstrated that applying this new approach to the existing catchment-wide ERT dataset measured with an ES of 2 m contributes to an improved characterization of the regolith. From a hydrological perspective, the deployment of the upgrading procedure at catchment scale is promising as it could bring new insights in terms of hydrological process understanding and modelling. Indeed, in the past years several investigations have pointed out the critical role of the Weierbach subsurface in its hydrological functioning (Pfister et al., 2010, 2017; Fenicia et al., 2014; Wrede et al., 2015; Martínez-Carreras et al., 2015, 2016; Scaini et al., 2017, 2018). Recently, using a 3D integrated hydrological surface–subsurface modelling approach, Glaser et al. (2019) were able to bring further evidences that the multi-layered nature – with contrasting hydraulic properties and effective conductivities – of the Weierbach regolith is responsible for the main processes controlling the hydrometric response in the catchment, i.e. fast vertical flow in the unsaturated zone combined with connected fast lateral subsurface flow. However, although the subsurface plays a key role in the hydrological functioning of the Weierbach catchment, its spatial variability has been taken into account only minimally for the moment. In the most recent hydrological model of the catchment, for example, the spatial variability of the

subsurface is only considered in the stream valleys, where solum and subsolum were eroded and the outcropping fractured bedrock is overlain with organic material (elsewhere in the catchment, the subsurface structure and properties were parameterized homogenously; Glaser et al., 2020).

Yet the intrusive point-scale investigation suggests a potentially significant spatial variability of the subsurface hydraulic properties (in close relation to the observed soil clay content, subsolum slate fragment size and bedrock weathering heterogeneity; see Sect. 2.1.1) that might be derived from the catchment-wide ERT survey as suggested in this study (see Sect. 3.2.1). Moreover, as highlighted by Loritz et al. (2017) in a nearby catchment with the same regolith structure, the bedrock topography plays a significant role in the interplay of water flow and storage in our study area. Using a physically based hillslope modelling approach, they showed that a model with surface-parallel bedrock topographies performed considerably worse in matching streamflow than a model including a bedrock topography. Furthermore, in their model, the topography of the bedrock was successfully constrained with an ERT survey using an ES of 0.5 m (Loritz et al., 2017), thus also underlining the added value that can be expected from the upgrading approach proposed in this study.

The presented elements suggest that the application of the upgrading procedure to the catchment-wide ERT survey dataset relying on an ES of 2 m constitutes a promising added value that might improve the model realism of the Weierbach catchment (Clark et al., 2017). We further expect that our novel approach may also be transferable to catchments with similar characteristics, like forested catchments with similar bedrock geology (e.g. Bellot and Ortiz de Urbina, 2008; Hübner et al., 2015). Specifically, the regolith of the Weierbach catchment is representative of the slate regolith which covers a large part of the Rhenish Massif (Moragues-Quiroga et al., 2017). Hence, we anticipate that the proposed protocol could be used in several regions of this large central European geological area that extends from Luxembourg through Belgium, France and Germany (Sauer and Felix-Henningsen, 2006).

5   Summary and conclusions

In catchment studies, our understanding of the mechanistics and prediction of subsurface water flow paths, transit times and storage volumes remains fractionate, largely as a result of our poor knowledge on regolith structure and characteristics. The characterization of the subsurface is stymied by the invasive and "point-scale" characters of traditional investigation techniques, essentially because of time and cost constraints. ERT is one of the geophysical tools at hand to overcome this limitation. This technique is now commonly used in the critical zone to disentangle regolith properties and architecture, but its use should go hand in hand with a suitable resolution of ERT images.

In this paper, we discuss the importance of ESs for the quality of ERT images to adequately mirror subsurface resistivity distributions and accurately delineate interfaces. To this end, we investigated a synthetic "conductive–resistive–conductive" three-layered sequence of soil–saprock/saprolite–bedrock, which mirrors the subsurface of many natural contexts, in combination with the Weierbach catchment field dataset, as a reference case study. Inversion results obtained for different ESs were compared in terms of resistivity distribution accuracy. We also inferred interface depths from each ERT image using a derivative method and evaluated their accuracy.

Our results highlight the need to use an adapted vertical resolution to best mirror the structure of the subsurface. More specifically, we document the inverse solution reconstruction issues related to the lack of shallow apparent resistivity data induced by the use of an oversized ES. We found out that the thickness of the most superficial layer must be taken into consideration when choosing the ES. Specifically, we demonstrated that the best compromise consists of using an ES close to the thickness of the subsurface top layer. If a larger ES is retained, the accuracy of the results decreases rapidly in terms of both resistivity distribution and interface delineation. This choice, which is obvious for the characterization of the shallower layer, is also relevant for characterizing the subsurface in its entirety – even when solely aiming for the characterization of deeper layers. For instance, our observations obviously support previous findings and confirm that oversizing the ESs not only leads to an inappropriate vertical resolution for the delineation of thin surface layers, but that it also affects the outlining of deeper layers. In particular, we demonstrated that an oversized ES leads to overestimations of the depth to bedrock and that this overestimation is even more important for subsurface structures with high resistivity contrast.

To overcome this limitation, we propose adding interpolated levels of surficial apparent resistivity based on a limited number of ERT profiles with a small ES that satisfies the thickness of the top subsurface layer. We show that our protocol significantly improves the accuracy of ERT profiles based on large ESs provided that the top layer has a rather constant thickness and resistivity, such as the solum in the Weierbach catchment. Our results demonstrated that this upgrading procedure is promising for carrying out large-scale surveys in a cost-effective and more robust way, for instance to feed hydrological models with subsurface structure depths and properties at catchment scale. However, our findings and their interpretation result from one typical regolith logic, and extra work is needed to strengthen, and eventually adapt, our upgrading approach to a more general regolith pattern. We especially recommend assessing the proposed methodology for the reverse case "resistive solum–conductive subsolum–resistive bedrock".

References

Abdullah, F. M., Loke, M. H., Nawawi, M., and Abdullah, K.: Assessing the reliability and performance of optimized and conventional resistivity arrays for shallow subsurface investigations, J. Appl. Geophys., 155, 237–245, 2018.

Ahrens, J., Geveci, B., and Law, C.: ParaView: An End-User Tool for Large Data Visualization, in: Visualization Handbook 2005, edited by: Hansen, C. D. and Johnson, C. R., Butterworth-Heinemann, 717–731, https://doi.org/10.1016/B978-012387582-2/50038-1, 2005.

Alamry, A. S., van der Meijde, M., Noomen, M., Addink, E. A., van Benthem, R., and de Jong, S. M.: Spatial and temporal monitoring of soil moisture using surface electrical resistivity tomography in Mediterranean soils, Catena, 157, 388–396, 2017.

Allroggen, N., Beiter, D., and Tronicke, J.: Ground-penetrating radar monitoring of fast subsurface processes, Geophysics, 85, 19–23, 2020.

Ameli, A. A., Amvrosiadi, N., Grabs, T., Laudon, H., Creed, I. F., McDonnell, J. J., and Bishop, K.: Hillslope permeability architecture controls on subsurface transit time distribution and flow paths, J. Hydrol., 543, 17–30, 2016.

Andersen, T. R., Poulsen, S. E., Christensen, S., and Jørgensen, F.: A synthetic study of geophysics-based modelling of groundwater flow in catchments with a buried valley, Hydrogeol. J., 21, 491–503, 2013.

Andrenelli, M. C., Magini, S., Pellegrini, S., Perria, R., Vignozzi, N., and Costantini, E. A. C.: The use of the ARP© system to reduce the costs of soil survey for precision viticulture, J. Appl. Geophys., 99, 24–34, 2013.

Archie, G. E.: The electrical resistivity log as an aid in determining some reservoir characteristics, Petroleum Transactions of AIME, 146, 54–62, 1942.

Audebert, M., Clément, R., Touze-Foltz, N., Günther, T., Moreau, S., and Duquennoi, C.: Time-lapse ERT interpretation methodology for leachate injection monitoring based on multiple inversions and a clustering strategy (MICS), J. Appl. Geophys., 111, 320–333, 2014.

Barker, R. D.: Depth of investigation of collinear symmetrical four-electrode arrays, Geophysics, 54, 1031–1037, 1989.

Bauer, P., Supper, R., Zimmermann, S., and Kinzelbach, W.: Geoelectrical imaging of groundwater salinization in the Okavango Delta, Botswana, J. Appl. Geophys., 60, 126–141, 2006.

Bellot, J. and Ortiz de Urbina, J. M.: Soil water content at the catchment level and plant water status relationships in a Mediterranean *Quercus ilex* forest, J. Hydrol., 357, 67–75, 2008.

Bennett, N. D., Croke, B. F. W., Guariso, G., Guillaume, J. H. A., Hamilton, S. H., Jakeman, A. J., Marsili-Libelli, S., Newham, L. T. H., Norton, J. P., Perrin, C., Pierce, S. A., Robson, B., Seppelt, R., Voinov, A. A., Fath, B. D., and Andreassian, V.: Characterising performance of environmental models, Environ. Modell. Softw., 40, 1–20, 2013.

Binley, A. and Kemna, A.: DC resistivity and induced polarization methods, in: Hydrogeophysics, edited by: Rubin, Y. and Hubbard, S. S., Springer, New York, 129–156, 2005.

Binley, A., Hubbard, S. S., Huisman, J. A., Revil, A., Robinson, D. A., Singha, K., and Slater, L. D.: The emergence of hydrogeophysics for improved understanding of subsurface processes over multiple scales, Water Resour. Res., 51, 3837–3866, 2015.

Brooks, P. D., Chorover, J., Fan, Y., Godsey, S. E., Maxwell, R. M., McNamara, J. P., and Tague, C.: Hydrological partitioning in the critical zone: Recent advances and opportunities for developing transferable understanding of water cycle dynamics, Water Resour. Res., 51, 6973–6987, 2015.

Brosten, T. R., Day-Lewis, F. D., Schultz, G. M., Curtis, G. P., and Lane, J. W.: Inversion of multi-frequency electromagnetic induction data for 3D characterization of hydraulic conductivity, J. Appl. Geophys., 73, 323–335, 2011.

Brunet, P., Clément, R., and Bouvier, C.: Monitoring soil water content and deficit using Electrical Resistivity Tomography (ERT) – A case study in the Cevennes area, France, J. Hydrol., 380, 146–153, 2010.

Burt, T. P. and McDonnell, J. J.: Whither field hydrology? The need for discovery science and outrageous hydrological hypotheses, Water Resour. Res., 51, 5919–5928, 2015.

Carrière, S. D., Chalikakis, K., Sénéchal, G., Danquigny, C., and Emblanch, C.: Combining Electrical Resistivity Tomography and Ground Penetrating Radar to study geological structuring of karst Unsaturated Zone, J. Appl. Geophys., 94, 31–41, 2013.

Carrière S. D., Chalikakis, K., Danquigny, C., and Torres-Rondon, L.: Using resistivity or logarithm of resistivity to calculate depth of investigation index to assess reliability of electrical resistivity tomography, Geophysics, 82, 93–98, 2017.

Cassidy, R., Comte, J. C., Nitsche, J., Wilson, C., Flynn, R., and Ofterdinger, U.: Combining multi-scale geophysical techniques for robust hydro-structural characterisation in catchments underlain by hard rock in post-glacial regions, J. Hydrol., 517, 715–731, 2014.

Chambers, J. E., Wilkinson, P. B., Wardrop, D., Hameed, A., Hill, I., Jeffrey, C., Loke, M. H., Meldrum, P. I., Kuras, O., Cave, M., and Gunn, D. A.: Bedrock detection beneath river terrace deposits using three-dimensional electrical resistivity tomography, Geomorphology, 177–178, 17–25, 2012.

Chambers, J. E., Wilkinson, P. B., Penn, S., Meldrum, P. I., Kuras, O., Loke, M. H., and Gunn, D. A.: River terrace sand and gravel deposit reserve estimation using three-dimensional electrical resistivity tomography for bedrock surface detection, J. Appl. Geophys., 93, 25–32, 2013.

Chambers, J. E., Wilkinson, P. B., Uhlemann, S., Sorensen, J. P. R., Roberts, C., Newell, A. J., Ward, W. O. C., Binley, A., Williams, P. J., Gooddy, D. C., Old, G., and Bai, L.: Derivation of lowland riparian wetland deposit architecture using geophysical image analysis and interface detection, Water Resour. Res., 50, 5886–5905, 2014.

Chambers, J. E., Meldrum, P. I., Wilkinson, P. B., Ward, W., Jackson, C., Matthews, B., Joel, P., Kuras, O., Bai, L., Uhlemann, S., and Gunn, D.: Spatial monitoring of groundwater drawdown and rebound associated with quarry dewatering using automated time-lapse electrical resistivity tomography and distribution guided clustering, Eng. Geol., 193, 412–420, 2015.

Clark, M. P., Bierkens, M. F. P., Samaniego, L., Woods, R. A., Uijlenhoet, R., Bennett, K. E., Pauwels, V. R. N., Cai, X., Wood, A. W., and Peters-Lidard, C. D.: The evolution of process-based hydrologic models: historical challenges and the collective quest for physical realism, Hydrol. Earth Syst. Sci., 21, 3427–3440, https://doi.org/10.5194/hess-21-3427-2017, 2017.

Clément, R., Descloitres, M., Günther, T., Ribolzi, O., and Legchenko, A.: Influence of shallow infiltration on time-lapse ERT: Experience of advanced interpretation, C. R. Geosci., 341, 886–898, 2009.

Clément, R., Bergeron, M., and Moreau, S.: COMSOL multiphysics modelling for measurement device of electrical resistivity in laboratory test cell, European Comsol Conference, 26–28 October 2011, Stuttgart, Germany, 2011.

Clément, R., Moreau, S., Henine, H., Guérin, A., Chaumont, C., and Tournebize, J.: On the value of combining surface and cross-borehole ERT measurements to study artificial tile drainage processes, Near Surf. Geophys., 12, 763–775, 2014.

Comte, J. C. and Banton, O.: Cross-validation of geo-electrical and hydrogeological models to evaluate seawater intrusion in coastal aquifers, Geophys. Res. Lett., 34, 1–5, 2007.

Comte, J. C., Cassidy, R., Nitsche, J., Ofterdinger, U., Pilatova, K., and Flynn, R.: The typology of Irish hard-rock aquifers based on an integrated hydrogeological and geophysical approach, Hydrogeol. J., 20, 1569–1588, 2012.

Comte, J. C., Ofterdinger, U., Legchenko, A., Caulfield, J., Cassidy, R., and Mezquita Gonzalez, J. A.: Catchment-scale heterogeneity of flow and storage properties in a weathered/fractured hard rock aquifer from resistivity and magnetic resonance surveys: implications for groundwater flow paths and the distribution of residence times, Geological Society, London, Special Publications, 479, 35–58, 2018.

Crook, N., Binley, A., Knight, R., Robinson, D. A., Zarnetske, J., and Haggerty, R.: Electrical resistivity imaging of the architecture of substream sediments, Water Resour. Res., 44, 1–11, 2008.

Dahlin, T. and Zhou, B.: A numerical comparison of 2D resistivity imaging with 10 electrode arrays, Geophys. Prospect., 52, 379–398, 2004.

Day-Lewis, F. D., Singha, K., and Binley, A.: Applying petrophysical models to radar travel time and electrical resistivity tomograms: resolution-dependent limitations, J. Geophys. Res., 110, 1–17, 2005.

Demoulin, A., Barbier, F., Dekoninck, A., Verhaert, M., Ruffet, G. Dupuis, C., and Yans, J.: Erosion Surfaces in the Ardenne–Oesling and Their Associated Kaolinic Weathering Mantle, in: Landscapes and Landforms of Belgium and Luxembourg, World Geomorphological Landscapes, edited by: Demoulin, A., Springer, Cham, 63–84, 2018.

Fan, B., Liu, X., Zhu, Q., Qin, G., Li, J., Lin, H., and Guo, L.: Exploring the interplay between infiltration dynamics and Critical Zone structures with multiscale geophysical imaging: A review, Geoderma, 374, 114431, 1–16, 2020.

Fan, Y., Clark, M., Lawrence, D. M., Swenson, S., Band, L. E., Brantley, S. L., Brooks, P. D., Dietrich, W. E., Flores, A., Grant, G., Kirchner, J. W., Mackay, D. S., McDonnell, J. J., Milly, P. C. D.l, Sullivan, P. L., Tague, C., Ajami, H., Chaney, N., Hartmann, A., Hazenberg, P., McNamara, J., Pelletier, J., Perket, J., Rouholahnejad-Freund, E., Wagener, T., Zeng, X., Beighley, E., Buzan, J., Huang, M., Livneh, B., Mohanty, B. P., Nijssen, B., Safeeq, M., Shen, C., van Verseveld, W., Volk, J., and Yamazaki, D.: Hillslope hydrology in global change research and Earth system modeling, Water Resour. Res., 55, 1737–1772, 2019.

Farzamian, M., Monteiro Santos, F. A., and Khalil, M. A.: Application of EM38 and ERT methods in estimation of saturated hydraulic conductivity in unsaturated soil, J. Appl. Geophys., 112, 175–189, 2015.

Fenicia, F., Kavetski, D., Savenije, H. H. G., Clark, M. P., Schoups, G., Pfister, L., and Freer, J.: Catchment properties, function, and conceptual model representation: Is there a correspondence?, Hydrol. Process., 28, 2451–2467, 2014.

Freer, J., McDonnell, J. J., Beven, K. J., Peters, N. E., Burns, D. A., Hooper, R. P., Aulenbach, B., and Kendall, C.: The role of bedrock topography on subsurface storm flow, Water Resour. Res., 38, 51–516, 2002.

Furman, A., Ferré, T. P. A., and Warrick, A. W.: Optimization of ERT surveys for monitoring transient hydrological events using perturbation sensitivity and genetic algorithms, Vadose Zone J., 3, 1230–1239, 2004.

Furman, A., Ferré, T. P. A., and Heath, G. L.: Spatial focusing of electrical resistivity surveys considering geologic and hydrologic layering, Geophysics, 72, 65–73, 2007.

Gabrielli, C. P., McDonnell, J. J., and Jarvis, W. T.: The role of bedrock groundwater in rainfall-runoff response at hillslope and catchment scales, J. Hydrol., 450–451, 117–133, 2012.

Ghasemizade, M. and Schirmer, M.: Subsurface flow contribution in the hydrological cycle: Lessons learned and challenges ahead-a review, Environ. Earth Sci., 69, 707–718, 2013.

Glaser, B., Klaus, J., Frei, S., Frentress, J., Pfister, L., and Hopp, L.: On the value of surface saturated area dynamics mapped with thermal infrared imagery for modeling the hillslope-riparian-stream continuum, Water Resour. Res., 52, 8317–8342, 2016.

Glaser, B., Jackisch, C., Hopp, L., and Klaus, J.: How meaningful are plot-scale observations and simulations of preferential flow for catchment models?, Vadose Zone J., 18, 1–18, 2019.

Glaser, B., Antonelli, M., Hopp, L., and Klaus, J.: Intra-catchment variability of surface saturation – insights from physically based simulations in comparison with biweekly thermal infrared image observations, Hydrol. Earth Syst. Sci., 24, 1393–1413, https://doi.org/10.5194/hess-24-1393-2020, 2020.

Graham, C. B., Woods, R. A., and McDonnell, J. J.: Hillslope threshold response to rainfall: (1) A field based forensic approach, J. Hydrol., 393, 65–76, 2010.

Guerrero, O., Lataste, J. F., and Marache, A.: High sampling rate measurement and data treatment for mobile investigations: Kinematic Electrical Resistivity Tomography (KERT), Geoderma, 284, 22–33, 2016.

Günther, T. and Rücker, C.: Boundless electrical resistivity tomography – BERT 2 – the user tutorial, available at: http://www.resistivity.net, last access: 24 March 2016.

Günther, T., Rücker, C., and Spitzer, K.: Three-dimensional modelling and inversion of DC resistivity data incorporating topography – II. Inversion, Geophys. J. Int., 166, 506–517, 2006.

Guo, L., Lin, H., Fan, B., Nyquist, J., Toran, L., and Mount, G. J.: Preferential flow through shallow fractured bedrock and a 3D fill-and-spill model of hillslope subsurface hydrology, J. Hydrol., 576, 430–442, 2019.

Gupta, H. V., Kling, H., Yilmaz, K. K., and Martinez, G. F.: Decomposition of the mean squared error and NSE performance criteria: Implications for improving hydrological modelling, J. Hydrol., 377, 80–91, 2009.

Hare, D. K., Boutt, D. F., Clement, W. P., Hatch, C. E., Davenport, G., and Hackman, A.: Hydrogeological controls on spatial patterns of groundwater discharge in peatlands, Hydrol. Earth Syst. Sci., 21, 6031–6048, https://doi.org/10.5194/hess-21-6031-2017, 2017.

Hastie, T., Tibshirani, R., and Friedman, J.: The Elements of Statistical Learning: Data Mining, Inference, and Prediction, 2nd edn., Springer, New York/Berlin/Heidelberg, 2008.

Hauduc, H., Neumann, M. B., Muschalla, D., Gamerith, V., Gillot, S., and Vanrolleghem, P. A.: Efficiency criteria for environmental model quality assessment: A review and its application to wastewater treatment, Environ. Modell. Softw., 68, 196–204, 2015.

Hirsch, M., Bentley, L. R., and Dietrich, P.: A comparison of electrical resistivity, ground penetrating radar and seismic refraction results at a river terrace site, J. Environ. Eng. Geoph., 13, 325–333, 2008.

Holbrook, W. S., Riebe, C. S., Elwaseif, M., Hayes, J. L., Basler-Reeder, K., Harry, D. L., Malazian, A., Dosseto, A., Hartsough, P. C., and Hopmans, J. W.: Geophysical constraints on deep weathering and water storage potential in the Southern Sierra Critical Zone Observatory, Earth Surf. Proc. Land., 39, 366–380, 2014.

Hopp, L. and McDonnell, J. J.: Connectivity at the hillslope scale: Identifying interactions between storm size, bedrock permeability, slope angle and soil depth, J. Hydrol., 376, 378–391, 2009.

House, A. R., Thompson, J. R., Sorensen, J. P. R., Roberts, C., and Acreman, M. C.: Modelling groundwater/surface water interaction in a managed riparian chalk valley wetland, Hydrol. Process., 30, 447–462, 2016.

Hsu, H. L., Yanites, B. J., Chen, C. C., and Chen, Y. G.: Bedrock detection using 2D electrical resistivity imaging along the Peikang River, central Taiwan, Geomorphology, 114, 406–414, 2010.

Hübner, R., Heller, K., Günther, T., and Kleber, A.: Monitoring hillslope moisture dynamics with surface ERT for enhancing spatial significance of hydrometric point measurements, Hydrol. Earth Syst. Sci., 19, 225–240, https://doi.org/10.5194/hess-19-225-2015, 2015.

Jackisch, C., Angermann, L., Allroggen, N., Sprenger, M., Blume, T., Tronicke, J., and Zehe, E.: Form and function in hillslope hydrology: in situ imaging and characterization of flow-relevant structures, Hydrol. Earth Syst. Sci., 21, 3749–3775, https://doi.org/10.5194/hess-21-3749-2017, 2017.

Juilleret, J., Iffly, J. F., Pfister, L., and Hissler, C.: Remarkable Pleistocene periglacial slope deposits in Luxembourg (Oesling): pedological implication and geosite potential, Bulletin de la Société des Naturalistes Luxembourgeois, 112, 125–130, 2011.

Juilleret, J., Dondeyne, S., Vancampenhout, K., Deckers, J., and Hissler, C.: Mind the gap: A classification system for integrating the subsolum into soil surveys, Geoderma, 264, 332–339, 2016.

Keller, G. V. and Frischknecht, F. C.: Electrical methods in geophysical prospecting, Pergamon Press, New York, 1966.

Kunetz, G.: Principles of direct current resistivity prospecting, Gebrüder Borntraeger, Geopublication Associates, Berlin, Germany, 1966.

Lanni, C., McDonnell, J. J., Hopp, L., and Rigon, R.: Simulated effect of soil depth and bedrock topography on near-surface hydrologic response and slope stability, Earth Surf. Proc. Land., 38, 146–159, 2013.

Leopold, M., Völke, J., Huber, J., and Dethier, D.: Subsurface architecture of the boulder creek critical zone observatory from electrical resistivity tomography, Earth Surf. Proc. Land., 38, 1417–1431, 2013.

Leslie, I. N. and Heinse, R.: Characterizing soil-pipe networks with pseudo-three-dimensional resistivity tomography on forested hillslopes with restrictive horizons, Vadose Zone J., 12, 1–10, 2013.

Lin, H.: Earth's Critical Zone and hydropedology: concepts, characteristics, and advances, Hydrol. Earth Syst. Sci., 14, 25–45, https://doi.org/10.5194/hess-14-25-2010, 2010.

Loke, M. H. and Barker, R. D.: Practical techniques for 3D resistivity surveys and data inversion, Geophys. Prospect., 44, 499–523, 1996.

Loke, M. H., Ackworth, I., and Dahlin, I.: A comparison of smooth and blocky inversion methods in 2D electrical imaging surveys, Explor. Geophys., 34, 182–187, 2003.

Loke, M. H., Chambers, J. E., Rucker, D. F., Kuras, O., and Wilkinson, P. B.: Recent developments in the direct-current geoelectrical imaging method, J. Appl. Geophys., 95, 135–156, 2013.

Loke, M. H., Wilkinson, P. B., Uhlemann, S. S., Chambers, J. E., and Oxby, L. S.: Computation of optimized arrays for 3-D electrical imaging surveys, Geophys. J. Int., 199, 1751–1764, 2014.

Loritz, R., Hassler, S. K., Jackisch, C., Allroggen, N., van Schaik, L., Wienhöfer, J., and Zehe, E.: Picturing and modeling catchments by representative hillslopes, Hydrol. Earth Syst. Sci., 21, 1225–1249, https://doi.org/10.5194/hess-21-1225-2017, 2017.

Marr, D. and Hildreth, E.: Theory of edge-detection, P. Roy. Soc. Lond. B Bio., 207, 187–217, 1980.

Martínez-Carreras, N., Wetzel, C. E., Frentress, J., Ector, L., McDonnell, J. J., Hoffmann, L., and Pfister, L.: Hydrological connectivity inferred from diatom transport through the riparian-stream system, Hydrol. Earth Syst. Sci., 19, 3133–3151, https://doi.org/10.5194/hess-19-3133-2015, 2015.

Martínez-Carreras, N., Hissler, C., Gourdol, L., Klaus, J., Juilleret, J., Iffly, J. F., and Pfister, L.: Storage controls on the generation of double peak hydrographs in a forested headwater catchment, J. Hydrol., 543, 255–269, 2016.

Mastrocicco, M., Vignoli, G., Colombani, N., and Abu Zeid, N.: Surface electrical resistivity tomography and hydrogeological characterization to constrain groundwater flow modeling in an agricultural field site near Ferrara (Italy), Environ. Earth Sci., 61, 311–322, 2010.

Meads, L. N., Bentley, L. R., and Mendoza, C. A.: Application of electrical resistivity imaging to the development of a geologic model for a proposed Edmonton landfill site, Can. Geotech. J., 40, 551–558, 2003.

Moragues-Quiroga, C., Juilleret, J., Gourdol, L., Pelt, E., Perrone, T., Aubert, A., Morvan, G., Chabaux, F., Legout, A., Stille, P., and Hissler, C.: Genesis and evolution of regoliths: Evidence from trace and major elements and Sr-Nd-Pb-U isotopes, Catena, 149, 185–198, 2017.

Nash, J. and Sutcliffe, J.: River flow forecasting through conceptual models part I – a discussion of principles, J. Hydrol., 10, 282–290, 1970.

Nguyen, F., Garambois, S., Jongmans, D., Pirard, E., and Loke, M. H.: Image processing of 2D resistivity data for imaging faults, J. Appl. Geophys., 57, 260–277, 2005.

Parsekian, A. D., Singha, K., Minsley, B. J., Holbrook, W. S., and Slater, L.: Multiscale geophysical imaging of the critical zone, Rev. Geophys., 53, 1–26, 2015.

Pfister, L., McDonnell, J. J., Hissler, C., and Hoffmann, L.: Ground-based thermal imagery as a simple, practical tool for mapping saturated area connectivity and dynamics, Hydrol. Process., 24, 3123–3132, 2010.

Pfister, L., Martínez-Carreras, N., Hissler, C., Klaus, J., Stewart, M. K., and McDonnell, J. J.: Bedrock geology controls on catchment storage, mixing and release: a comparative analysis of 16 nested catchments. Hydrol. Process., 31, 1828–1845, 2017.

Rejiba, F., Schamper, C., Chevalier, A., Deleplancque, B., Hovhannissian, G., Thiesson, J., and Weill, P.: Multiconfiguration electromagnetic induction survey for paleochannel internal structure imaging: a case study in the alluvial plain of the River Seine, France, Hydrol. Earth Syst. Sci., 22, 159–170, https://doi.org/10.5194/hess-22-159-2018, 2018.

Reynolds, J. M.: An introduction to applied and environmental geophysics, 2nd edn., John Wiley and Sons, Oxford, United Kingdom, England, 2011.

Robinson, D. A., Binley, A., Crook, N., Day-Lewis, F. D., Ferré, T. P. A., Grauch, V. J. S., Knight, R., Knoll, M., Lakshmi, V., Miller, R., Nyquist, J., Pellerin, L., Singha, K., and Slater, L.: Advancing process-based watershed hydrological research using near-surface geophysics: A vision for, and review of, electrical and magnetic geophysical methods, Hydrol. Process., 22, 3604–3635, 2008.

Roy, A. and Apparao, A.: Depth of investigation in direct current methods, Geophysics, 36, 943–959, 1971.

Rücker, C., Günther, T., and Spitzer, K.: Three-dimensional modelling and inversion of DC resistivity data incorporating topography I. Modelling, Geophys. J. Int., 166, 495–505, 2006.

Saey, T., De Smedt, P., Islam, M. M., Meerschman, E., Van De Vijver, E., Lehouck, A., and Van Meirvenne, M.: Depth slicing of multi-receiver EMI measurements to enhance the delineation of contrasting subsoil features, Geoderma, 189–190, 514–521, 2012.

Šamonil, P., Phillips, J., Daněk, P., Beneš, V., and Pawlik, L.: Soil, regolith, and weathered rock: Theoretical concepts and evolution in old-growth temperate forests, Central Europe, Geoderma, 368, 114261, https://doi.org/10.1016/j.geoderma.2020.114261, 2020.

Sauer, D. and Felix-Henningsen, P.: Saprolite, soils, and sediments in the Rhenish Massif as records of climate and landscape history, Quatern. Int., 156–157, 4–12, 2006.

Scaini, A., Audebert, M., Hissler, C., Fenicia, F., Gourdol, L., Pfister, L., and Beven, K. J.: Velocity and celerity dynamics at plot scale inferred from artificial tracing experiments and time-lapse ERT, J. Hydrol., 546, 28–43, 2017.

Scaini, A., Hissler, C., Fenicia, F., Juilleret, J., Iffly, J. F., Pfister, L., and Beven, K. J.: Hillslope response to sprinkling and natural rainfall using velocity and celerity estimates in a slate-bedrock catchment, J. Hydrol., 558, 366–379, 2018.

Schoeneberger, P. J. and Wysocki, D. A.: Hydrology of soils and deep regolith: A nexus between soil geography, ecosystems and land management, Geoderma, 126, 117–128, 2005.

Simon, F. X., Pareilh-Peyrou, M., Buvat, S., Mayoral, A., Labazuy, P., Kelfoun, K., and Tabbagh, A.: Quantifying multiple electromagnetic properties in EMI surveys: A case study of hydromorphic soils in a volcanic context – The Lac du Puy (France), Geoderma, 361, 114084, 2020.

Singha, K.: Geophysics Is Not a Silver Bullet, but Worth a Shot, Groundwater, 55, 149–149, 2017.

Slater, L.: Near surface electrical characterization of hydraulic conductivity: From petrophysical properties to aquifer geometries – A review, Surv. Geophys., 28, 169–197, 2007.

Sponton, H. and Cardelino, J.: A Review of Classic Edge Detectors, Image Processing On Line, 5, 90–123, 2015.

Stummer, P., Maurer, H., and Green, A. G.: Experimental design: Electrical resistivity data sets that provide optimum subsurface information, Geophysics, 69, 120–139, 2004.

Tetegan, M., Pasquier, C., Besson, A., Nicoullaud, B., Bouthier, A., Bourennane, H., Desbourdes, C., King, D., and Cousin, I.: Field-scale estimation of the volume percentage of rock fragments in stony soils by electrical resistivity, Catena, 92, 67–74, 2012.

Torreão, J. R. A. and Amaral, M. S.: Efficient, recursively implemented differential operator, with application to edge detection, Pattern Recogn. Lett., 27, 987–995, 2006.

Tran, A. P., Dafflon, B., Hubbard, S. S., Kowalsky, M. B., Long, P., Tokunaga, T. K., and Williams, K. H.: Quantifying shallow subsurface water and heat dynamics using coupled hydrological-thermal-geophysical inversion, Hydrol. Earth Syst. Sci., 20, 3477–3491, https://doi.org/10.5194/hess-20-3477-2016, 2016.

Uhlemann, S. S., Sorensen, J. P. R., House, A. R., Wilkinson, P. B., Roberts, C., Gooddy, D. C., Binley, A. M., and Chambers, J. E.: Integrated time-lapse geoelectrical imaging of wetland hydrological processes, Water Resour. Res., 52, 1607–1625, 2015.

Uhlemann, S., Wilkinson, P. B., Maurer, H., Wagner, F. M., Johnson, T. C., and Chambers, J. E.: Optimized survey design for electrical resistivity tomography: Combined optimization of measurement configuration and electrode placement, Geophys. J. Int., 214, 108–121, 2018.

Velde, B. and Meunier, A.: The origin of clay minerals in soils and weathered rocks, Springer, Berlin, 406 p, 2008.

Wainwright, H. M., Flores Orozco, A., Bücker, M., Dafflon, B., Chen, J., Hubbard, S. S., and Williams, K. H.: Hierarchical Bayesian method for mapping biogeochemical hot spots using induced polarization imaging, Water Resour. Res., 52, 533–551, 2016.

Ward, W. O. C., Wilkinson, P. B., Chambers, J. E., Oxby, L. S., and Bai, L.: Distribution-based fuzzy clustering of electrical resistivity tomography images for interface detection, Geophys. J. Int., 197, 310–321, 2014.

Wilkinson, P. B., Meldrum, P. I., Chambers, J. E., Kuras, O., and Ogilvy, R. D.: Improved strategies for the automatic selection of optimized sets of electrical resistivity tomography measurement configurations, Geophys. J. Int., 167, 1119–1126, 2006.

Wilkinson, P. B., Loke, M. H., Meldrum, P. I., Chambers, J. E., Kuras, O., Gunn, D. A., and Ogilvy, R. D.: Practical aspects of applied optimized survey design for electrical resistivity tomography, Geophys. J. Int., 189, 428–440, 2012.

Wrede, S., Fenicia, F., Martínez-Carreras, N., Juilleret, J., Hissler, C., Krein, A., Savenije, H. H. G., Uhlenbrook, S., Kavetski, D., and Pfister, L.: Towards more systematic perceptual model development: a case study using 3 Luxembourgish catchments, Hydrol. Process., 29, 2731–2750, 2015.